Structure and conformational variability of the HER2-trastuzumab-pertuzumab complex

Rémi Ruedas, Rémi Vuillemot, Thibault Tubiana, Jean-Marie Winter, Laura Pieri, Ana-Andreea Arteni, Camille Samson, Slavica Jonic, Magali Mathieu, Stéphane Bressanelli

Structure and conformational variability of the HER2-trastuzumab-pertuzumab complex

Rémi Ruedas[1,2,*], Rémi Vuillemot[4], Thibault Tubiana[1], Jean-Marie Winter[3], Laura Pieri[1], Ana-Andreea Arteni[1], Camille Samson[2], Slavica Jonic[4], Magali Mathieu[2], Stéphane Bressanelli[1,+]

[1] Université Paris-Saclay, CEA, CNRS - Institute for Integrative Biology of the Cell (I2BC), 91198, Gif-sur-Yvette, France.
[2] Sanofi, Integrated Drug Discovery, 13, quai Jules Guesde, 94403 Vitry-sur-Seine, France
[3] NanoImaging Core Facility, Centre de Ressources et Recherches Technologiques (C2RT), Institut Pasteur, 75015 Paris, France.
[4] IMPMC-UMR 7590 CNRS, Sorbonne Université, Muséum National d'Histoire Naturelle, 75005 Paris, France
[+]To whom correspondence shoud be addressed: stephane.bressanelli@i2bc.paris-saclay.fr
[*]Present address: Basel University, Biozentrum, Spitalstrasse 41, 4056 Basel

Abstract

Single particle analysis from cryogenic transmission electron microscopy (cryo-EM) is particularly attractive for complexes for which structure prediction remains intractable, such as antibody-antigen complexes. Here we obtain the detailed structure of a particularly difficult complex between human epidermal growth factor receptor 2 (HER2) and the antigen-binding fragments from two distinct therapeutic antibodies binding to distant parts of the flexible HER2, pertuzumab and trastuzumab (HTP). We highlight the strengths and limitations of current data processing software in dealing with various kinds of heterogeneities, particularly continuous conformational heterogeneity, and in describing the motions that can be extracted from our dataset. Our HTP structure provides a more detailed view than the one previously available for this ternary complex. This allowed us to pinpoint a previously overlooked loop in domain IV that may be involved both in binding of trastuzumab and in HER2 dimerization. This finding may contribute to explain the synergistic anticancer effect of the two antibodies. We further propose that the flexibility of the HTP complex, beyond the difficulties it causes for cryo-EM analysis, actually reflects regulation of HER2 signaling and its inhibition by therapeutic antibodies. Notably we obtain our best data with ultra-thin continuous carbon grids, showing that with current cameras their use to alleviate particle misdistribution is compatible with a protein complex of only 162 kDa. Perhaps most importantly, we provide here a dataset for such a smallish protein complex for further development of software accounting for continuous conformational heterogeneity in cryo-EM images.

Keywords

Antibody-antigen complex; HER2 signaling; cryogenic electron microscopy; continuous conformational variability

1 Introduction

Human epidermal growth factor receptor 2 (HER2 or ErbB2) plays a critical role in cell signaling and its deregulation is involved in many cancers. It is a member of the ErbB family of tyrosine kinase receptors. There are four receptors in the family: epidermal growth factor (EGF) receptor 1 (also termed ErbB1/HER1), ErbB2/Neu/HER2, ErbB3/HER3 and ErbB4/HER4. ErbB receptors can form homo- and heterodimers mediated by EGF-related peptide growth factors that bind to their extracellular domain [1]. No ligand has been identified for HER2, and even if some papers suggest that it can form homodimers [2][3], it is more commonly described as the favored heterodimerization partner for the other ErbB receptors [4] [5] [3]. The heterodimers involving HER2 have higher signaling potency than heterodimers involving other ErbB receptors [4]. HER2-involving signaling is directly linked with cell growth and, when HER2 is overexpressed, with several cancers. Pro-oncogenic HER2 heterodimers with other HER receptors form through HER2 extracellular region (hereafter sHER2), leading to autophosphorylation of its intracellular region and downstream signaling. Dimerization and pro-oncogenic effects can be inhibited by antibodies directed against sHER2, prominently two monoclonal anti-sHER2 antibodies, trastuzumab (Herceptin) and pertuzumab (Perjeta). Trastuzumab binds to domain IV of sHER2 (see below) and was first approved by the Food and Drug Administration [6] and by the European Medicine Agency (EMA) in 2000 for its use against HER2-positive breast cancer [7]. Fab (Fragment antigen binding) related effects of trastuzumab are manyfold and include cytostatic effect, angiogenic factor regulation, antibody-mediated aggregation [8] and internalization of HER2. Trastuzumab also inhibits a proteolytic cleavage of HER2 to a shorter form p59HER2 that is active in signaling [9]. Its Fc related effects are antibody-dependent cellular cytotoxicity (ADCC) and IgG1 half-life increasing, the latter being important for favorable trastuzumab pharmacokinetics. However, acquired trastuzumab resistance has appeared over time, which needs to be overcome [10]. Pertuzumab has taken this role. Like trastuzumab, pertuzumab is a HER2 targeting humanized monoclonal antibody. It was first approved by the FDA in 2012 [11] and by the EMA in 2013 [12]. Pertuzumab binds to domain II of sHER2 and its main Fab effect is to sterically block the HER2 dimerization process [13]. Combination of trastuzumab and pertuzumab displays a synergistic effect [13–15] and therefore is currently used as a very effective immunotherapy strategy against breast cancer [16–19].

Accordingly, the molecular basis of trastuzumab and pertuzumab inhibition of HER2 has been the subject of much basic research. Particularly the atomic structures of complexes of sHER2 with Fabs have been reported (Table 1), first by X-ray crystallography for sHER2-trastuzumab [20] and for sHER2-pertuzumab [21]. In recent years HER2 structural biology has taken advantage of the ongoing revolution in cryogenic electron microscopy (cryo-EM) to provide atomic-level structures of large protein complexes. Thus, several important cryo-EM structures of HER2 complexes have been solved by single particle analysis (SPA), particularly the HER2-HER3 and HER2-HER3-trastuzumab (Fab) complexes [22]. A major conclusion of these recent works is that dynamics are important for HER2 dimerization and for regulation of signaling [22,23]. However, these dynamics also make HER2 complexes difficult objects for SPA: Not only is sHER2 only 630 residues (70 kDa, not counting glycosylations), but its complexes tend to display several kinds of heterogeneity. This includes continuous conformational variability, that is currently the object of much research in the data processing cryo-EM community [24,25]. Thus, the only structure of the tripartite complex between sHER2, trastuzumab Fab and pertuzumab Fab (hereafter called the HTP complex) is available only to lowish resolution (Table 1) and in particular does not allow visualizing to atomic resolution the HER2-trastuzumab interface, as this interface lies in the most flexible and least resolved part of HTP [26].

The architecture of HER extracellular regions includes four domains, consecutive in sequence, I to IV (Fig. 1a). In sHER2, domains I, II and III pack together while IV forms an elongated stem that connects to the transmembrane helix in full-length HER2. Accordingly, in maps of sHER2 but also of solubilized full-length HER2, the tip of IV is poorly defined and most residues beyond 570 are not resolved, including residues close to the trastuzumab paratope. Indeed, in cryo-EM SPA the most encountered limiting factors are particles distribution and orientation, ice thickness, and sample flexibility [27–31].

As to particles' distribution and orientation, there is a well-known and unpredictable gap between sample preparation and the vitrification process. Often particles are strongly affected by the air-water interface and the more widely used approaches to overcome the associated problems of particle misdistribution and/or damage is to work on the water surface by adding detergent or to add a continuous thin carbon layer support [32–34].

Even if there is no foolproof method to predict the behavior of particles on the grids and during vitrification, an exhaustive quality assessment of the sample strongly increases success rates [35,36]. Here we use such an approach to present a complete cryo-EM structure of the HTP complex that allows simultaneously resolving all HER2-trastuzumab and HER2-pertuzumab interactions. By using state-of-the-art image processing methods, we account for intrinsic flexibility of the complex and describe both its structure and motion.

2 Results

2.1 An exhaustive biophysical view of the HTP complex

The HTP complex was formed and purified by a protocol adapted from Hao et al, 2019, with a final size exclusion chromatography step to separate the full complex from free Fabs (see 'Materials and methods'). On the day freshly FPLC-purified samples were vitrified on grids, their integrity and suitability for cryo-EM were checked by UV-spectroscopy, dynamic light scattering (DLS) and differential scanning fluorimetry (nano-DSF) measurements. Good HTP samples were devoid of detectable chemical contamination (absorbance ratio 260nm/280nm were below 0.6) and had a low aggregation index (Ai = $\frac{100 * A340}{A280 - A340} < 2$). The size variation induced by the binding of 2 fabs (Δ100kDa) on sHER2 was enough to induce a significant change in the diffusion coefficient measured by DLS and thus in the apparent hydrodynamic radius from 3.2nm (±0.22), 3.34nm (±0.46) and 4.61nm (±0.11) for trastuzumab Fab, pertuzumab Fab and sHER2 respectively to 6.19 (±0.34) for the HTP ternary complex (Supp. Fig. 1). Systematic nano-DSF measurements gave direct information about the complex stability in solution through the melting temperature, that can be inferred from the variations in fluorescence (Tm) or light scattering (Tscatt) as temperature is increased. In isolation, both Fabs showed much higher light scattering counts and apparent size ($1E^8$ counts, rh~1000nm) than sHER2 ($6E^6$ counts; rh~10nm), indicating that Fabs aggregated upon denaturation (Supp. Fig. 1). While isolated sHER2 displayed one melting point (Tm 67 °C), two melting points were observed for the HTP complex, confirming that the first (69 °C) and second (80 °C) melting points for HTP correspond to sHER2 and the Fabs, respectively. The Tm of sHER2 increased from 67°C in isolation to 69°C in the HTP complex, consistent with sHER2 stabilization by the two Fabs (Supp. Fig. 1).

The sample was further characterized by static light scattering coupled to size exclusion chromatography (SEC-SLS). The sample eluted at 0.3mg/ml (1.8 µM) had a mass of ~171 kDa, indicating the HTP complex was formed and stable at this concentration (Supp. Fig. 1).

Mass-photometry was also performed on a frozen-thawed sample. Mass photometry is a single-molecule technique that applies the principle of interference reflection microscopy and

interferometric scattering microscopy to quantify light scattered by molecules on a glass coverslip [37]. This experiment revealed five populations (Supp. Fig. 3, bottom right). The first three major peaks had apparent weights consistent with the HTP trimer, a "binary" complex probably formed by a single Fab complexed with sHER2 and a free population of Fabs. Finally, two higher weight peaks were also apparent, one barely visible at around 340 kDa and the other a substantial part of the counts (23%) at 685 kDa. The latter one is also visible by DLS, as a sharp increase in polydispersity in frozen-thawed samples from a low value of the polydispersity index of 0.07 (±0.02) for the fresh sample (Supp. Fig. 2). In stability tests performed by negative staining microscopy, frozen-thawed sample particles do appear different from fresh sample particles (Supp. Fig. 2), even though they remain well distributed and concentrated. Still the different populations observed by mass photometry on the frozen-thawed complex could be explained in part by the working concentration of 10 nM that could be close to the dissociation constants of the Fabs, since Kds for the full antibodies were reported in the low nanomolar range by enzyme linked immunosorbent assay (1.43 nM for trastuzumab, 1.92 nM pertuzumab) [38]. To distinguish the effect of dilution from that of freeze-thawing, we again used mass photometry but this time on fresh samples (Supp. Fig. 3, bottom left panel, top panels). We found nothing above the molecular weight of HTP this time. Indeed at 21 nM of freshly purified HTP, the full complex was the major peak, while at higher dilutions a ~50-kDa peak corresponding to dissociated Fab became more pronounced. We used this observation to estimate the binding affinities of each Fab to sHER2 by mixing sHER2 with one Fab at a time and measuring the relative numbers of free Fab, free sHER2 and binary complexes HT or HP. We found dissociation constants of around 1 nM for trastuzumab and around 2 nM for pertuzumab (Table 2).

To conclude, DLS, mass photometry and negative staining EM indicate that the HTP complex is stable at the micromolar concentrations we used for cryo-EM (see below), but that freeze-thaw cycles tend to induce dissociation and aggregation of HTP. Thus cryo-EM grids were prepared only from fresh samples.

2.2 Grid type strongly impacts particles behavior and proved to be the critical factor to reach high resolution in cryo-EM SPA

HTP samples at a typical concentration of 0.1-0.3 mg/ml were applied on grids and plunge-frozen (see Materials and Methods and Table 4). Grids screening was performed according to hierarchical criteria. First the grids overall quality (*e.g.* grid and ice integrity and a good thickness gradient along the grid), then the ice quality including amorphous state and relative thickness (visually assessed), finally the particles' distribution in thin ice. The HTP particle is too small for integrity and/or orientation bias to be checked by direct visualization. Thus, the only visual quality criteria were the particles' density and distribution over the holes. Our grid screening strategy is schematized in supplementary figure 4.

Data were collected and processed as described in Material and methods and table 4. The major differences according to grid type are summarized in supplementary figure 5 and 6. According to sample characterization, there was no reason to think that aggregation would be a concern with a freshly prepared sample. However, when we used the published conditions for cryo-EM grid preparation of HTP on quantifoil grids [26], we experienced difficulties in reproducibly obtaining well-dispersed complexes in thin ice. Indeed, when using classic quantifoil grids, particle clustering repeatedly and vexingly appeared upon blotting and plunge-freezing grids despite numerous biochemical screening trials (Table 3 & Supp. Fig. 5). A low-resolution reconstruction of the HTP trimer could still be made from such a grid. However, 3D classification revealed that besides the full HTP trimer, there was a subpopulation where trastuzumab was missing. Further exhaustive image analysis using deep particle picking revealed that the HTP complex is furthermore also present as a doublet occurring by self-association through two parallel pertuzumab Fabs (Supp. Fig. 5). Map quality for the

doublet does not allow to precisely identify which amino acids are involved in this self-association, but it is good enough to fit atomic models that show that i) pertuzumab-pertuzumab contacts occur through the variable regions, but opposite the pertuzumab paratope and ii) the elbow angle (angle between variable and constant regions) is different from the (average) one in the free HTP complex. This doublet could be one of the building blocks of the clusters that are the main factor impairing high resolution reconstruction in classic quantifoil grids.

We therefore tested gold grids called UltrAufoil. No aggregation/clustering are visible on those grids, but partially assembled complex forms are present (Supp. Fig. 5). Four different objects can be reconstructed. Two of them can be unequivocally attributed to the full ternary complex HTP and the partially assembled complex pertuzumab-sHER2, as on the classic quantifoil grid. The third and fourth volumes appear smaller and could correspond to a partially assembled complex trastuzumab-sHER2 and unbound Fabs or noise. Thus, UltrAufoil grids helped with the HTP complex' dispersion in ice but not with its integrity. The sample heterogeneity and the ice thickness severely limited the resolution on these grids during our exhaustive data processing. We did not find the doublet found on classic quantifoil grids in UltrAufoil grids or other grid types, despite extensive searches using the same protocols as for classic quantifoils and going to 2d classification and ab initio volume generation. As the doublet was readily visible in 2D classification for classic quantifoils, we conclude that it is not found in appreciable quantities in other grid types. At any rate, this in-depth analysis shows that objects detected after freeze-thawing by mass photometry (both incomplete complexes and doublets) and DLS (higher order aggregates) can actually be found in ice after plunge-freezing a fresh sample (Supp. Fig. 2, 3 & 5).

In view of this we next played with different factors that could further improve sample quality upon vitrification. This included grid material but also grid treatment, varying biochemical conditions and blotting time and force prior to plunge-freezing (Table 3). Each condition was tested in duplicate for a total of some eighty grids. Using ultrathin carbon coated (UTC) quantifoil grids was the critical factor that finally allowed to have undamaged and well-distributed HTP particles in thin ice (Supp. Fig. 5, lower panel). In the commercial grids we used, the additional carbon layer was mostly broken, making most grids unusable. But with one of the few undamaged UTC grids we could obtain a 3D reconstruction to an overall resolution of about 3.3 Å, compared to the previous 4.4 Å [26]. The three reconstructions obtained for the HTP complex and associated metrics are summarized in supplementary figure 6.

2.3 Complete, simultaneous atomic description of both HTP epitope-paratope interfaces: a fourth loop in the trastuzumab paratope

The map clearly shows that the standard image analysis protocol used (hereafter the baseline protocol, see methods) allows accurate reconstruction of the I to III part of sHER2 and the variable region of the bound Pertuzumab Fab (both the part coming from the heavy chain V_H and from the light chain V_L) (Fig. 1a). However, the map is of much lower quality in the region comprising sHER2 IV and the trastuzumab Fab. We further ran two focused refinements, one in a mask including sHER2 domains I to III and the pertuzumab Fab (Fig. 1b), and the other including most of sHER2 domain IV and the trastuzumab Fab (Fig. 1c) and combined the two focused maps (Fig. 1d). Focused refinement further improved the map even in the pertuzumab region, with an overall resolution of 3.0 Å and a local resolution reaching 2.5 Å almost throughout this whole subpart of the combined map (Fig. 1b). In fact, the interface between HER2 and pertuzumab is better defined than in the available crystal structure (Table 1). We can thus ascertain that this interface is the same as in that former structure (Fig. 2b) [21], with only minor changes. This confirms that simultaneous binding of trastuzumab does not affect the HER2-pertuzumab interface, as previously reported [26]. Focused refinement particularly improved

the trastuzumab region (Fig. 1c). Focused refinement there reports an overall resolution of 3.3 Å, and the map is very clear in the HER2-trastuzumab interface. To describe it, we use the same numbering as in the initial sHER2-trastuzumab crystal structure [20], *i.e.* starting the sHER2 sequence at residue 1 and not counting the 22-residue signal peptide of the HER2 ORF. The HER2-trastuzumab interface thus involves at its center the hydrophobic HER2 bulge 570-573 and on either side loop 557-561 and some residues of 593-603, in agreement with the crystal structure (Fig. 2a, yellow). However in this region our maps also show clear features of a fourth, long HER2 loop 581-590 involved in the interface (Fig. 1, Fig. 2a, purple). Particularly residues D585-S587 at its tip make contact to a trastuzumab surface contributed by several CDR's (complementarity-determining regions as defined in Ling et al. [39]): a cleft of the heavy chain at the bottom of which is R98 and lined by CDR's H3 and H1 and an aromatic patch provided by the light chain CDR L2 (Fig. 2a). Density in this region was actually present if barely visible in Hao et al. and Diwanji et al. cryoEM maps, supporting our decision to redefine the HER2 trastuzumab binding surface as a four-part epitope (Fig. 2). A summary of residues involved in the two interfaces sHER2-trastuzumab and sHER2-pertuzumab is given in table 5.

2.4 Continuous conformational variability analysis

The combined focused map is still less good in the Trastuzumab region than in the Pertuzumab region (Fig. 1d). This may be due in part to the fact that Pertuzumab Fab together with domains I, II and III of HER2 account for 941 amino acids (61.5% of the complex) against only 587 amino acids (38,5%) for HER2 domain IV and Trastuzumab Fab, making the smaller region more difficult to align. But this is also the most flexible region of the HTP complex and is likely not well described by a single conformation. Indeed, 3D classification without alignment (that is, using the alignments computed in the baseline refinement, see Material and methods) converged to roughly equally populated classes with distinct conformations and no incomplete class (not shown, we tried up to ten classes), suggesting that heterogeneity in the "UTC quantifoil" dataset is continuous rather than discrete. We therefore applied specific image processing protocols that seek to account for continuous conformational variability in cryo-EM images.

2.4.1 3DFlex from cryoSPARC

We thus used the newly released 3D Flexible Refinement (3DFlex)[25] of cryoSPARC [40]. 3DFlex, a motion-based deep neural network model of continuous heterogeneity, extracts a latent space of continuous motion from 2D image data to learn non-rigid motions. The outputs of 3DFlex are on the one hand series of volumes describing the motions and on the other hand a single 'canonical' reconstructed map from 'back-deformed' images to recover high-resolution details of flexible parts. As the current 3DFlex beta version is demanding on computational resources, we first applied 3DFlex on a 286,008 particles subset (hereafter 286k subset) of the full 711,008 particles dataset previously obtained as described in Material and methods. As we had a few strongly favored orientations in the dataset, we did not select a random subset but made a python script RSPFilter, to specifically remove particles in the most favored orientations while keeping all particles from less populated orientations (Supp. Fig. 7). The 3DFlex canonical map reconstructed from this subset of particles shows a marked improvement in the trastuzumab region compared to the map obtained with the baseline protocol (Figure 3a). This suggests that the latent space extracted by 3DFlex is correct and thus that it was successful in capturing the conformational landscape in the 286k subset. Indeed, the main motions generated by the 3DFlex flow generator show several major modes that are consistent with the expected dynamics of the complex, namely flexibility around hinge regions: The elongated domain IV of HER2 on the one hand and the elbow regions of Fabs on the other hand.

Thus, the three main motions are located, with increasing amplitude and complexity, in the hinge between the constant and variable regions of pertuzumab, in the equivalent hinge of trastuzumab,

and in HER2 domain IV (Figure 3c). It is particularly noteworthy that despite considerable motion in IV, the four-part trastuzumab epitope remains associated, seemingly without change, with the long IV loop 581-590 engaged to Trastuzumab in all conformations. Thus the apparent disorder that had precluded its identification as part of the epitope in the initial crystal structure (Cho *et al.*, 2003) does not seem to be due to local flexibility of this loop. To better ascertain these points, we next applied the same 3DFlex protocol to the full 711,008 particle dataset. However, the additional particles led to a dampening of the motions generated by 3DFlex, though the motions were qualitatively the same as output for the 286k RSPFiltered subset. We tried changing several different parameters such as 2 to 5 latent dimensions during Flex train, initializing with latent coordinates from 3D Variability Analysis, using a segmentation file during Flex mesh prep, or cropping and downsampling to different extents during Flex data prep. The only parameter that had some effect was the extent of cropping applied prior to Flex train, as tighter boxes generally led to less dampened motions. For instance, cropping the box from 230pix (266.3 Å) to 200 pix during Flex data prep increased the amplitude of movements both for the 286k subset and the full 711k dataset. Nevertheless, the resulting movements were still dampened for the full dataset. The largest distance beween extremes in conformations was in the constant region of trastuzumab and reached ~21 Å for the RSPFiltered 286k dataset (Figure 3c) while it remained below 5 Å for the full dataset. Accordingly, although the 3DFlex canonical map presents much better features in the less mobile pertuzumab region with the full dataset than with the 286k subset, it is actually degraded in the trastuzumab region (Figure 3a-b). In view of this we went back to the baseline reconstruction protocol and the two focused refinements with the 286k subset only, to see if a similar improvement could be obtained. However, the maps were of lesser quality than with the full dataset. Interestingly, the effect was severe with the baseline reconstruction, where resolution dropped from 3.3 to ~4 Å, but not so much with the focused maps. Thus the map focused on the pertuzumab Fab and HER2 I-II-III still reached a resolution of 3.2 Å (3 Å with the full dataset), while the map focused on the trastuzumab Fab and HER2 IV reached a resolution of 3.7 Å (3.3 Å with the full dataset). A summary of all maps generated from this dataset is given in table 6.

2.4.2 MDSPACE

3DFlex has the advantage that it learns the continuous conformational variability directly from the dataset, but the disadvantage that prior knowledge in the form of an atomic model cannot be input or guide the search, even in such a difficult case as HTP. To probe the validity of the 3DFlex results and better assess the continuous conformational variability of the HTP complex, we therefore used a different approach, the recently published MDSPACE [24]. Molecular Dynamics simulation for Single Particle Analysis of Continuous Conformational heterogeneity (MDSPACE) uses an atomic model of the complex as input (here, the model built from the data) and applies a per-particle flexible fitting using MD simulations to match the conformation in each particle image. The flexible fitting uses and normal mode empowered MD simulation to accelerate the process in an iterative scheme that helps to extract the conformations from projections where the flexibility is more difficult to discern (particularly particles viewed along the direction of one of the main movements). A coarse-grained or atomic-level conformation is thus assigned to each particle in the dataset. As shown in Figure 3D, using the whole dataset and a coarse-grained HTP model, the MDSPACE analysis identified major movements that are very similar to those resulting from the 3DFlex analysis, particularly in the HER2/trastuzumab region. However, the movements from MDSPACE are of greater amplitude (47 Å between extremes) than from 3DFLex, even when comparing with the 286k subset 3DFlex analysis (compare Fig. 3D with Fig. 3C).

Despite the less restricted conformational space described, the MDSPACE coarse-grained models do not show variation of the HER2-trastuzumab interface. However, the coarse-grained Go model used in the analysis imposes geometric constraints on the structure that may not allow detecting local

flexibility, such as a single loop motion. Therefore, to overcome this limitation, inherent to the use of coarse-grained Go-model MD simulations, we performed a second MDSPACE analysis using the all-atom HTP model and the classical, physics-based MD forcefield CHARMM, on a smaller dataset for computational reasons (a subset of 5k particles). This all-atom model was able to capture local dynamics, but aligning the resulting all-atom models on trastuzumab shows that the interface with HER2 still remains stable (Fig. 3E, right). The main local motion in this region is around the Fab's elbow angle between the constant and variable regions (Fig. 3E, left). Thus, all continuous conformational variability analyses, including the MDSPACE all-atom approach, consistently show the stability of the fourth part of the HER2-trastuzumab interface (loop 581-590 with CDR's H3, L1 and L2).

3 Discussion

Our study sheds further light on the simultaneous molecular interactions of trastuzumab and pertuzumab with HER2. We propose the involvement of a fourth interaction point between trastuzumab and HER2 domain IV. This fourth part of the sHER2 trastuzumab epitope, loop 581-590, had actually been built in the lower resolution map of the HTP complex, albeit in a different conformation (PDB 6oge), but it is not mentioned in the paper [26]. Our flexibility analysis shows that loop 581-590 is an integral part of the trastuzumab-HER2 interface in all distinguishable conformations of the HTP complex. This loop completes the striking likeness between the epitopes of trastuzumab in domain IV and pertuzumab in domain II. In the HER2 modular architecture, domain IV is a repeat of domain II and loop 581-590 in domain IV is the counterpart of the "dimerization arm" in domain II. Both contain hydrophobic bulges that in the case of the dimerization arm is known to be involved in the heterodimerization process [21–23,41]. The close resemblance between the binding sites of trastuzumab and pertuzumab suggests a common mechanism of binding, while their synergistic effect on HER2 signaling[13–15] hints that different processes are inhibited by the two antibodies. Interestingly, the domain IV loop in HER2, although it is not clearly defined in any experimental map except ours (Fig. 2), would fall near the domain IV loop in HER3 in the HER2-HER3 complex. In contrast, the two domains IV are further apart in the HER2-HER3-trastuzumab complex, precluding any interaction between their loops upon trastuzumab binding, although HER2 and HER3 remain associated through the dimerization arm in domain II [22]. This may hint at a signaling mechanism in which both the 581-590 loop in domain IV and the dimerization arm in domain II are required. Finally, a bibliographic survey of the copious litterature on HER2 inhibition by and resistance to trastuzumab shows that, although most resistance arises from outright deletion of sHER2 or disruption of downstream signaling, some minor modifications of sHER2 can also have a profound effect [42]. One particularly interesting resistant variant is the so-called ' d16HER2 splice variant', that forms stable and constitutively active homodimers on the tumor cell surface [43]. The only difference with HER2 is that d16HER2 misses the 16 residues 612-627 (634–649 counting the 22-residue signal peptide). In our HTP structure these residues form a platform, stabilized by disulfide bridges C620-C604 and C612-C608, that directly interacts with the base of loop 581-590, including I591 and Y588. This variant thus further points to the involvement of this region in both trastuzumab interaction and HER2 dimerization.

Our study supports the typical workflow and troubleshooting in cryo-EM, especially the gap between the "on the bench" sample preparation and characterization and finding a suitable vitrification process avoiding the twin problems of dissociation and aggregation. Although current cryo-EM software allows a rapid data processing, we would like to emphasize again the advantages of a solid sample biophysical characterization prior to or concurrently with the cryo-EM steps. Not only does it give a useful (though never foolproof) indication of the most likely sample conditions for good vitrification, but it also allows a better understanding of the observations in the cryogenic electron microscope. In the case of the HTP complex, a particularly difficult complex for cryo-EM, we show that fine characterization by mass

photometry, DLS and negative staining EM observations of frozen/thawed or aged samples actually detect the dissociated or aggregated states that occur in unsatisfactory vitrification processes. We also confirm that the stability and dispersion of the biological sample during vitrification is intricately linked to the grid material and find, by trial and error, that an ultrathin carbon coating on the grid is the crucial factor for a satisfactory vitrification of the HTP complex. This is somewhat surprising as UTC grids, though widely used to mitigate air-water interface problems for large complexes, are usually described as less suitable for complexes below 300 kDa. For small complexes, graphene or graphene oxide grids, although fragile and difficult to handle properly, are preferred as they do not introduce as much background noise as the amorphous carbon layer of UTC grids. In our hands the principal problem with purchased UTC grid was broken layers of carbon. It may be worthwhile to keep in cryo-EM labs the expertise to prepare home-made UTC grids by adding a thin film of carbon on top of conventional grids, to circumvent the problem of unreliable commercial grids and to obtain a thinner carbon that is most suitable for high-resolution SPA cryo-EM. We show here that, with careful sample characterization and with current microscope and camera performance, even (good) commercial UTC grids are actually suitable for a 162-kDa protein complex and should not be disregarded beforehand.

Finally, we make available to the community a dataset that offers several advantages for further method development in protein studies by cryo-EM. It is of a smallish, compositionally homogeneous object with a distinct shape, large continuous conformational variability, and a strong orientation bias while still sampling all orientations. We provide a user-friendly utility, RSPFilter, to analyze and mitigate the effects of orientation bias in cryo-EM data and a concrete example of its usefulness and interest. Using this dataset, we show that two state-of-the-art software packages for conformational variability analysis perform differently in the challenges posed by this dataset. Particularly MDSPACE performs a finer analysis as it detects a wider range of motions, likely because it makes use of additional structural information (the atomic model built from the data). The smaller box size of our dataset compared to those typically used to benchmark such software offers a double advantage of less computational demand and the possibility of using the full resolution for images (without downsampling) and of working with atomic models. This makes it an ideal test case for further development of cryo-EM data processing software accounting for flexibility. Overall, our findings highlight the potential of our dataset for advancing methodology and software development in cryo-EM studies of flexible protein complexes.

4 Materials and Methods

4.1 Sample preparation

Human Her2 / ErbB2 ectodomain comprising residues Thr23-Thr652 of the HER2 open reading frame (numbered 1-627 in this study) followed by his tag was purchased as a lyophilized powder from ACROBIOSYSTEMS Inc (Cat. No. #HE2-H5212). It was resuspended in 10mM HEPES pH 7.5, 150mM NaCl and injected on a Superdex 200 increase 10/300 GL size exclusion column at 7°C. Fractions containing sHER2 were concentrated up to DO=3.2, aliquoted in 15 µL fractions, fast frozen in liquid nitrogen and stored at -80°C.

Monoclonal antibodies (mABs) pertuzumab and trastuzumab purchased from CliniSciences (Nanterre, France, Cat. No. HY-P9912 and HY-P9907) according to the supplier Pertuzumab and trastuzumab are recombinant humanized monoclonal antibody produced by recombinant DNA technology in a mammalian cell (Chinese Hamster Ovary) culture containing the antibiotic, gentamicin. Pertuzumab and Pertuzumab have an approximate molecular weight of 148 kDa. They were solubilized in sodium phosphate buffer at pH 7.5 at ~3mg/ml (DO~4.2) then aliquoted and stored at -20°C before digestion using commercial immobilized papain (#20341 Thermo Fisher Scientific) to produce Fabs. For

digestion, 250 µL of 50% immobilized papain were poured in a 1ml spin column (#69725 Thermo Fisher Scientific) and washed with ultrapure water using a benchtop centrifuge. Then the papain was activated and equilibrated with the digestion buffer containing 20mM cystein, 10 mM EDTA, 20 mM sodium phosphate pH 7.5. Monoclonal antibodies were complemented up to 20 mM cystein. Then the mAb was digested at 37°C during 4-5 hours under constant agitation using intelli-mixer to avoid papain beads sedimentation. After digestion, elution was done by several centrifugations at 1000g on an Eppendorf centrifuge. Fabs were purified from Fc and undigested IgG by ion exchange chromatography using 3 ml SP-Sepharose resin (#17-0729-10 GE-Healthcare). Before injection, Fabs were dialysed overnight at 7°C in 50mM Acetate buffer pH4 then injected in the SP-sepharose. Loading and washing steps were done in buffer A (50mM Acetate buffer pH4), elution was performed with a gradient of 40% buffer B (Buffer A + 1M NaCl) in 120 min at 0.3 ml/min. The first peak contains Fab, the second peak contains Fc and undigested IgG. Fractions containing the Fabs were neutralized with 1 M HEPES pH 7.5. Then they were buffer exchanged with 10 mM HEPES pH 7.5 and 150 mM NaCl by overnight dialysis at 7°C or by fast buffer exchange using centricon 30 kDa. They were concentrated up to ~1 ml and injected on a Superdex 200 10/300 GL size exclusion chromatography (SEC Citiva). Two SDS-PAGE 14% acrylamide with fractions of all steps were performed with and without reducing agent to visualize papain digestion and the purity of samples. Then they were concentrated up to DO=3.2, divided in 15 µL aliquots, fast frozen in liquid nitrogen and stored at -80°C.

Complex formation. The complex was formed by incubating the two Fab's (from trastuzumab and pertuzumab) with sHER2 on ice during around 5 minutes. The ratio was 1:1.2:1.2 sHER2/Fab1/Fab2. The complex was then purified through a S200 GE healthcare size exclusion chromatography in 10 mM HEPES pH 7.5 and 150 mM NaCl. A shift of peak corresponding to an increasing size of the object was obtained compared to the sHER2 alone and Fab alone injections.

4.2 Biophysical measurements

UV spectrum. 2.5 µL of the sample was deposited on the cell of a nano-drop spectrophotometer (nanodrop one Thermo Fisher Scientific) and a UV spectrum was recorded from 230nm to 350nm. Quality assessment is done as described in raynal et al. 2021 [36]

DLS & nano-DSF. Measures were performed on the prometheus panta from nanotemper. Samples were diluted to an OD 280 nm signal between 0.3 and 1 and centrifugated a 11 000*g* during 10 min. 10 µL were used to fill the capillary of the system and start the measurement. DLS measurement was performed at 15°C. DSF was measured on a ramp from 15°C to 95°C with steps of 0.5°C. Data were processed using the nano-temper software.

Mass photometry. Mass and relative abundance of species in HTP samples were measured using a TwoMP mass photometer (Refeyn Inc., Oxford, UK). A freshly purified HTP complex was use, or a frozen 1 month old HTP complex was thawed prior to deposition in the Refeyn cell. Sample was loaded on a silicone gasket (CultureWell™ reusable gasket, 3 mm diameter × 1 mm depth, Grace Bio-Labs) and placed onto clean glass coverslips (Refeyn Inc.). In each well, 10 µL of buffer (10mM MES pH6.5, 150 mM NaCl) was deposited and a blank measurement made. Subsequently, protein sample was mixed with the buffer in the well to a final concentration of ~10 nM. The molecular weight of the samples was assigned by contrast comparison of known mass standard calibrants measured on the same day. Dissociation constants were estimated using freshly purified proteins. Two separate solutions were made each containing one Fab mixed with an equimolar concentration of sHER2. Concentration was monitored throughout UV using a nanodrop. For the sHER-pertuzumab Fab complex, four dilutions were measured (4.3 nM, 8.6 nM, 13.1 nM and 26.2 nM) with a 1 min acquisition. The same protocol

was applied with the sHER2-trastuzumab Fab complex (4.6 nM, 9.2 nM, 13.8 nM and 27.7 nM). Dissociation constants were extracted according to the protocol described in Solterman et al [44].

SEC-SLS. Complex was prepared as described above and injected on a OMNISEC (Malvern Panalytical) with a Superdex 200 10/300 GL equilibrated in 10 mM HEPES pH 7.5 and 150 mM NaCl coupled with a static light scattering (SLS) detector.

Negative Staining. Freshly made complex was diluted 100 times and a 3µl drop placed on the grid. After 15 seconds the drop was dried with Whatman paper and then colored using 2% uranyl acetate. Images were acquired with a Tecnai Spirit 120 kV LaB6 (FEI) equipped with a K2 Base Direct Detection Camera (Gatan).

4.3 Cryo-EM grid preparation

Immediately before grid preparation, the grids were glow-discharged using GloQube plus system. Except for the ionization tests performed on quantifoils (table 3), the routine protocol for Quantifoil, UltrAufoil, UTC-Quantifoil and C-flat grids is 10-20 sec at 12 mA under vacuum. All grids were prepared by plunge freezing in liquid ethane using Vitrobot Mark IV system (Thermo Fisher Scientific, USA). Blotting parameters were adjusted for each session and depend on the vitrobot used. Usually, blotting time was near 4 seconds, blotting force 0 with no waiting time before blotting. Sample deposited was 2-3 µL with an OD 280 nm between 0.1 and 0.3 (table 4), in a humidity chamber kept at 100% for all grid preparation. The temperature did not impact the sample distribution on the grid, consistent with DSF and DLS measurements, and so the grids described in this paper were prepared at 15°C. During the procedure, sample was kept on ice. For the exhaustive data processing only the grids Quantifoil Cu 1.2/1.3µm 200 mesh, UltrAufoil 0.6/1µm 200 mesh and UTC+quantifoil Cu 1.2/1.3µm 200 mesh were used. All grids came from quantifoil company. The UTC-quantifoil grids refer to commercial quantifoil® grids with 2 nm carbon, lot n°Q81922. These commercial grids had their additional carbon layer mostly broken, but a few remained usable.

4.4 Cryo-EM data acquisition

All data collection parameters are summarized in table 4. The classic-Quantifoil and UTC-Quantifoil grid movies were recorded in eer format, UltrAufoil in tiff.

4.5 Data Processing

UTC Quantifoil. Processing is summarized in supplementary figure 8**.** Data were processed using Cryosparc v. 3.3.2 and v. 4.1.2 with 3DFlex. Eer movies format were imported with 54 eer fractions and an upsampling factor of 1.

Baseline protocol: All movies were motion corrected using patch motion correction multi with a F-crop factor of 0.5, using all frames (total dose 60 $\bar{e}/Å^2$). Then CTF estimation was done using Patch CTF estimation with default parameters. Micrographs were screened using curate exposure according to CTFfit, total full frame motion distance and average defocus values. Bad ice (cubic or hexagonal phase), blurred or empty images were then discarded. 2D templates for picking were obtained by a first automatic (blob) picking over 50 random micrographs followed by 2D classifications. A few good classes were used for template picking with a particle diameter of 160 Å and a minimum distance of 0.5. Coordinates were screened using inspect particle picks and the selected 2 954 825 particles were extracted in a box size on 280 pixels (i.e. 313.6 Å). After 2D classification, ab-initio volume generation was performed separately with particles from good and from bad 2D classes. The two 'good' volumes and three 'bad' volumes were used for successive rounds of heterogeneous refinement with increasing resolution, interspersed with homogeneous refinement of the best class. Particles were re-extracted once to recenter them in the box based on an intermediate homogeneous refinement (supp. Fig. 8).

This procedure yielded 742 378 particles in the best class. These particles were 2D-classified again and particles from noisy classes were discarded. The remaining 711 008 particles were CTF global and local refined in cryosparc, before being injected to a new homogeneous refinement yielding a map at an overall 3.3 Å resolution.

Local refinement: From this map two masks were created using ChimeraX and CryoSPARC map tools, one mask covering the pertuzumab Fab - HER2 domains I-II-III region and the other covering the trastuzumab Fab - HER2 domain IV region. Two distinct local refinements were done using those masks and all particles without re-splitting the particles into two gold standard halves.

Composite map building**:** Using Phenix software, the two local refinement maps were merged to create a composite map. We used the global homogeneous refinement map from the baseline protocol as input reference, a preliminary pdb model of the complex with two atom selections corresponding to the two masks of the local refinements (pertuzumab/sHER2 and trastuzumab/sHER2 regions, respectively), and then the map and half-maps for each local refinement. The resolution was set at 2.5 Å. The output of the algorithm is a composite map and the corresponding half-maps. These maps were converted into mrc format by chimeraX and then imported into cryosparc to calculate the GS-FSC and local resolution.

RSPFilter. We made a Python 3.8 script RSPFilter to analyze and filter a set of particles described in a STAR file. Particles are filtered using a grid density technique to create a more homogeneous repartition of the particles according to two properties selected in the STAR file. The star file Python package reads a STAR file and converts it into a Pandas Dataframe. The density (i.e. number of particles per square) is computed with the "binned_statistic_2D" function of Scipy package 1.9.3 [45] In each square, if the density is above a chosen density cutoff, particles are randomly eliminated until the density corresponds to the cutoff. Graphics are generated with the plotly package [46] and the web interface with Panel 0.14. RSPFilter is available on github (https://github.com/tubiana/RSPFilter), [47] and can be installed through pypi.

In the case of UTC quantifoil data, we first converted the Cryosparc files "*_particles.cs" and "*_passthrough_particles.cs" from *cs* format to *star* format with "csparc2star.py" from the pyem collection [48]. Then using RSPFilter we computed the two-dimensional particle density according to the rotation angle ("rlnAngleRot") and the tilt angle ("rlnAngleTilt") with a resolution of 3°. A cutoff of 254 yielded the 286k particle subset.

3DFlex. We ran the Cryosparc v. 4.1.2 3DFlex analysis on the full set of particles and on the 286k subset. The protocol for the results presented here involved cropping from 280 to 220 pixels and downsampling to 128 pixels in Flex data prep, adjusting mask threshold and dilation in Flex mesh prep to have a mesh generously covering the HTP complex map considering it potential flexibility (Threshold 0.1 and a mask dilation set at 5 Å for the 286k subset) and 5 latent dimensions in Flex train. Flex reconstruct was run with 60 BFGS iterations and force re-do GS split.

MDSPACE. The analysis of MDSPACE [24] was performed on particles that were cropped from 280 to 220 pixels and binned by 2 (final pixel size of 2.08 $Å^2$). Two different forcefields were used for the MD simulations in MDSPACE. The first is a coarse-grained Gō model including Cα atoms only, that was used to analyze the entire dataset of full set of particles and study the global variability. The second is the all-atom CHARMM forcefield which was used to analyze a random subset of 5k particles and study the local variability. In both cases, we used the atomic model derived from the combined map obtained with the two focused refinements as the initial conformation for the fitting. We also used the particle pose obtained by Cryosparc as the initial particle pose used for MDSPACE. The model was energy

minimized with each forcefield and the simulations were performed for 200 picoseconds with a time step of 2 femtoseconds using GENESIS [49]. The MD simulations were empowered using Normal Mode Analysis (NMA) through the NMMD [50] to accelerate the fitting. The normal modes were computed from the initial conformation using an elastic network model (ENM) as described in [24] and the four lowest frequency normal modes (mode 7 to 10 as the first six modes corresponds to rigid motions) were selected for the fitting. In the analysis of the full set of particles dataset using Cα-Gō model, MDSPACE was run for 2 iterations, with a first iteration (training) including a random subset of 1k particles, and the second iteration including the entire dataset and using the three principal motions learned from the previous iteration calculated by principal component analysis (PCA), through the iterative protocol described in the Vuillemot et al. 2013 paper. The fitted structures were rigid-body aligned with respect to the pertuzumab Fab of the initial conformation and projected onto a low-dimensional space using PCA. The low-dimensional space was used to obtain the presented averaged structures and the 3D reconstructions. For that, semi-automated clustering was performed on the PCA space by using the MDSPACE animation tool in Scipion [51], along the first three PCA components. The presented averaged structures were obtained by averaging the atomic coordinates of the fitted structures that belong to each cluster. The presented 3D reconstructions were obtained by performing 3D reconstruction on the particles contained in each cluster. In the analysis of 5k particles using CHARMM forcefield, MDSPACE was run for one single iteration. The fitted structures were rigid body aligned to the trastuzumab Fab and the atoms of the trastuzumab Fab and its interface were selected to calculate the root mean square fluctuation (RMSF) that measures the average variation of each residue of the 5000 fitted structures. The entire MDSPACE workflow was executed in the ContinuousFlex plugin [52] of Scipion [51].

Classic Quantifoil data processing. Two sets of eer movies (5566 and 5958) collected on the same microscope using the same data collection parameters were merged. Data were processed first with the baseline protocol with minor variations. The pixel size was 0,6 Å and 8 870 micrographs were kept after screening. From 683 895 particles found, 2D classification revealed the presence of a doublet of HTP complex in addition to HTP-sized particles. Thus, we used the deep picker topaz [53] to selectively find the doublet particles over the dataset. From 2D classification, a template showing the doublet was used for template picking over 1000 micrographs. The 79 594 extracted particles were Fourrier dowsampled by 2 (pixel size 1,12 Å) and screened by two successive 2D classifications retaining only classes showing a doublet. The remaining 1 286 particles and their associated micrographs were selected and used for topaz train. Training was done with a downsampling factor of 6 (effective pixel size of 3,6 Å) and an expected number of 10 particles per micrographs. Other parameters were kept as default. Topaz extract was performed over the whole set of screened micrographs with a radius of extracted regions set to 35 pixels. 151 242 particles were found and classified into three 3D classes using heterogeneous refinement and a pixel size of 2,5 Å (Voxel 144). Particles assigned to the doublet class were combined with those obtained with template picking. Duplicates were removed using a minimum separation distance of 50 Å.

A last round of heterogeneous refinement of the 755 345 particles with 4 volumes (HTP, Doublet, pertuzumab/sHER2 and trash/junk volume) with a pixel size of 4,7 Å (Voxel 72) followed by a NU-refinement for each class yields the maps shown in supplementary figure 5.

UltrAufoil data processing. A set of 5 637 tiff movies format with a pixel size of 0.86 Å were imported and process as describe in the baseline protocol except for minor variations. Template picking over all the remaining 4098 screened micrographs, led to 1 014 383 particles after an 'inspect particle picks' correction. from a that were extracted within a box size of 360 pixels binned to 120 pixels (effective pixel size of 2.58 Å). After 2D classification, ab-initio volume generation was performed separately with

particles from good and from bad 2D classes. Four 'good' volumes and two 'bad' volumes were used for three successive rounds of heterogeneous refinement with increasing resolution removing the particles from the 'junk' classes. 740 544 particles were kept for a last round of heterogeneous refinement that gives the 4 volumes shown in supplementary figure 5.

Model building. To initiate the reconstruction, we combined the pdb files from 1N8Z (trastuzumab) and 1S78 (pertuzumab) removing HER2 from 1S78. We built a *de-novo* extra cellular domain of HER2 using alphafold according to the sequence used (Thr23-Thr652). In Pymol, we aligned locally the alphafold model on the 1N8Z and completed the missing part with the alphafold model. The regions that were completed are Leu101-Ser111, Ala302-Thr306, Asp360-Ser365, and Ser580-Ile591, Asn607-Thr652.

Model refinement. The initial model was first fit in the density of the composite map and briefly overall refined using Isolde [54] in ChimeraX [55]. Then the model was refined in coot and phenix using alternatively the composite map from the two focused refinements and the global homogeneous refinement map at the end of the baseline protocol. The final phenix real space refinements were done in the global homogeneous refinement map. Model statistics are summarized in table 7.

DATA AVAILABILITY

The cryo-EM atomic model, maps used in refinement (global map, focused maps and composite map), and images have been deposited in the Protein Data Bank (ID code 8Q6J, 8PWH), Electron Microscopy Data Base, https://www.ebi.ac. uk/emdb/ (EMD-18188, EMD-18189, EMD-18190, EMD-EMD-17993), and Electron Microscopy Public Image Archive, https:// www.ebi.ac.uk/empiar/ (EMPIAR-11665.)

ACKNOWLEDGEMENTS

We wish to thank Malika Ould Ali from the I2BC Cryo-EM facility as well as Maelenn Chevreuil and Bertrand Raynal, from the Institut Pasteur, plateforme de biophysique moléculaire of C2RT. We acknowledge the cryo-EM platform nanoimaging of the institut Pasteur.

FUNDING INFORMATION

This work benefited from the CryoEM platform of I2BC, supported by the French Infrastructure for Integrated Structural Biology (FRISBI) [ANR-10-INSB-05-05] and from support of MOSBRI (European Union's Horizon 2020 research and innovation program under grant agreement No 101004806).

TT is the recipient of an ANRS-MIE postdoctoral fellowship ECTZ189696.

We acknowledge the support of the French National Research Agency - ANR (ANR-19-CE11-0008 to SJ) and access to HPC resources of IDRIS granted by GENCI (AD010710998R1 and AD010710998R2 to SJ).

5 Tables

PDB code	Description	Technique	Res. (A)	Date	Publication & authors
1s78	HER2/Pertuz	X-ray	3.25	2004	Insights into ErbB signaling from the structure of the ErbB2-pertuzumab complex [21]
1n8z	HER2/Tastuz	X-ray	2.52	2003	Structure of the Extracellular Region of HER2 Alone and in Complex with the Herceptin Fab [20]
7mn8	HER2/HER3/ NRG1β Trastuz	CryoEM	3.45	2021	Structures of the HER2-HER3-NRG1β complex reveal a dynamic dimer interface. [22]
6oge	HER2/Trastuz /Pertuz	CryoEM	4.36	2019	Cryo-EM structure of Her2 extracellular domain-Trastuzumab Fab-Pertuzumab Fab complex [26]
6bgt	HER2/Trastuz mutant	X-ray	2.7	2017	To be published (*Christie, M., Christ, D. not published*)
3be1	HER2/Trastuz (dual)	X-ray	2.9	2009	Dual specific bH1 Fab in complex with the extracellular domain of HER2/ErbB-2 [56]

Table 1. State of the art. All structures of HER2/Fab complexes available in the pdb prior to this work.

[HER2] and [pert] (nM)	**4.3**	**8.6**	**13.1**	**26.2**
Kd via trast counts (nM)	2.04	1.71	0.83	0.56

[HER2] and [trast] (nM)	**4.6**	**9.2**	**13.8**	**27.7**
Kd via pert counts (nM)	0.89	0.85	0.83	0.57

Table 2. Dissociation constant (Kd) analysis by mass photometry for sHER2-pertuzumab Fab (HP) and sHER2-trastuzumab Fab (HT) using the Soltermann et al. protocol. The values obtained at higher concentrations (>10xKd) are less robust as free species have too few counts and as the histograms overlap .

Overview of tested parameters			
Parameters		**Part. dist.**	
Grid treatment	5mM MgAc post-plasma, 10% Acetone, 10% EtOH, 10% SDS.	Fail	**Grids physics**
Blotting T°	4°C, 15°C, 22°C		
Vitrobot blotting parameters	Blotting times 2 to 8 seconds, blotting force –5 to +5, waiting time 0 to 10 seconds before and after		
Plasma cleaner	5-50mA 0-40sec		
Concentration	OD_{280nm}~0.3	Partial success (Supp. Fig. 5-6)	**Biochemical condition**
pH	4.3 – 7.5 - 9	Fail	
Salt	NaCl 30/150/300 mM		
Buffer detergent	SDS 0.2mM & 0.1%, Tween 20 0.1%, TritonX 0.01%		
Grids	Quantifoil (Cu, Au, C-Flat) & Lacey	Fail	**Grids Nature**
	UTC Quantifoil	**Success**	
	UltrAufoil	Partial success	

Table 3. Review of all grids and parameters screened for plunge-freezing and the impact on particles distribution. Not all combinations were tried, but overall > 60 grids were imaged. The quality criterion success/failure is assessed by visual inspection of test micrographs. Failed samples (aggregated or too sparsely included in ice) are not further analyzed. Subsequent data collection and processing is used to distinguish partial success (heterogeneity of apparently well-distributed sample precludes high resolution reconstruction) from actual success.

Grid type	OD_{280nm} [mg/ml] (µM)	Microscope	Data collection parameters					Median CTF	N° of particles	Map. Resolution	B-factor Å²
			N° of micrographs	Magnification	Camera	Pixel size Å/pix	Dose e/Å²				
UTC Quantifoil 1.2/1.3µm	0.15 [0.12] (0.73)	Glacios	8787	240k	Falcon 4	0.58	60	3.2Å	711 008	3.3Å	-130.2
UTC Quantifoil 1.2/1.3µm	0.34 [0.27] (1.6)	Glacios	1000	240k	Falcon 4	0.58	60	3.7Å	70 071	5.97Å	-374.4
QuantiFoil 300 1.2/1.3µm	0.3 [0.23] (1.45)	Glacios	8870	240k	Falcon 4i	0.60	50	3.5Å & 8.5Å	489 795	<6Å	-331
QuantiFoil 300 1.2/1.3µm	0,1 [0.08] (0.48)	Glacios	1448	120k	falcon 3	1.12	60	7.5Å	***	***	***
UltrAufoil 300 0.6/1 µm	0.1 [0.08] (0.48)	Titan Krios	4231	102K	Falcon 3i	0.86	60	3.8Å	740 544	6<Å<7.2	-741.3
UltrAufoil 300 R1.2/1.3 µm	0.1 [0.08] (0.48)	Glacios	1861	120k	Falcon3	1.12	60	7.5Å	91 501	7.4Å	-662.8

Table 4. Summary of data collection parameters and data processing results. Reconstructions obtained from the grids in bold are described in this article. The fourth column shows the number of micrographs (mic.) remaining after screening (usually by CTF fit resolution, but also by visual inspection). The fifth column gives the magnification used during data collection. The sixth column gives the pixel size of the RAW movies. The ninth column gives the median CTF value of the whole dataset and was determined visually according to the plot $CTFfit_{resolution}$=f(defocus) made in cryoSPARC (two values are given for a bimodal distribution). B-factor is given only for the global refinement.

Interfaces sHER2-Fabs	
sHER2	**Fab**
sHER2-trastuzumab interface	
(**1**) Asp560, Gln561, Pro557	**CDR H2** Arg50, Tyr57, Arg59
(**2**) Asp570, Pro572, Phe573, Lys593	**CDR H1** Tyr33, & **CDR H3** Trp99, Tyr105
(**3**) Trp592, Pro603 Glu602	**CDR H3** Phe104, Ala106, **CDR L2** Leu46, Tyr49, Tyr55, Phe53 **CDR L1** Asp30
(**4**) Asp585	**CDR H3,** Arg98
sHER2-pertuzumab interface	
(**1**) Leu244, His245	**CDR H2** Gly55
(**2**) Tyr252, Phe257, Thr254, Asp255	**CDR H2** Lys58, Tyr59, Gln61 & **CDR L3** Tyr94
(**3**) Val286, Thr290, Pro294, Leu295	**CDR H1** Thr33, Tyr32 & **CDR H3** Pro98, Leu96
(**4**) Ser288, Thr290	**CDR H1** Asp31**, CDR H2** Asp 53
(**5**) His286	**CDR H3** Tyr99B
(**6**) Pro315	**CDR L2** Tyr49, Tyr53

sHER2 domains & Fab CDRs		
Domain I: 1-185	**Domain III**: 320-485	**Pertuzumab :** CDR L1 (K24-A34); CDR L2 (S50-Y55); CDR L3 (Q89-T97); CDR H1 (G26-D35), CDR H2 (A49-G65), CDR H3 (A93-Y103)
Domain II: 186-219	**Domain IV**: 486-630	**Trastuzumab**: CDR L1 (R24-A34), CDR L2 (S50-Y55), CDR L3 (Q89-T97), CDR H1 (G26-H35), CDR H2 (R50-K65), CDR H3 (S97-Y109)

Table 5. Top, summary of the different epitope/paratope interfaces defined by the amino acids involved in the interactions. Bottom, definition of the HER2 domains and CDR of the two Fabs. CDR are defined according to *Ling et al.* [39]

		GS-FSC resolution *
Global refinement (after CTFrefine)	Global homogeneous refinement map	3.27Å
Local refinement (after CTFrefine)	sHER2-pertuzumab & sHER2-trastuzumab	3.05Å & 3.33Å
Composite map (combined using phenix)	combined from the local maps sHER2-pertuzumab & sHER2-trastuzumab Com	
3DFlex 711k ptcs (particles after ctf refinement)	3Dflex-711k	3.54Å
3DFlex 286k ptcs	3DFlex-286k	3.50Å

Table 6. Summary of the maps generated from the dataset collected on the UTC-Quantifoil grid and presented in the article. * for 3DFlex maps, resolution is estimated in real space.

	Ternary complex	
	Composite map	Global map
	(EMD-17993) (PDB 8pwh)	(EMD-18188) (PDB 8Q6J)
Data collection and Processing		
Microscope	Glacios	
Camera	Falcon 4	
Magnification	240k	
Voltage	200 kV	
Electron dose	60e/Å^2	
Defocus range (μm)	-0.8 to -2.6 (step 0.2)	
Pixel size (Å)	0.58Å/pixel	
Symmetry	C1	
Map resolution (0.143)	3.17 Å	3.27 Å
Mix resolution (Å)	< 2.5	
Particules		
Initial numbers of particles	2 954 825	
Final numbers of particles	711 008	
Refinement		
Initial model used	6oge, 1n8z, 1s78, alphafold	
Model composition		
Non-hydrogen atoms	11535	
Residues	Protein: 1494 Nucleotide: 0	
Ligands	BMA : 2 NAG : 7	
B-factors (Å) (min/max/mean)		
Protein	48.43/278.76/138.51	53.07/1018.44/225.27
Ligand	50.89/184.43/126.51	114.54/263.93/185.13
R.m.s deviations		
Bonds (RMSD)		
Bond Length (Å) (# > 4σ)	0.004 (0)	0.007 (0)
Angles (°) (# > 4σ)	0.612 (2)	0.735 (1)
Validation		
MolProbity score	2.65	2.90
Clash score	15.36	19.52
Ramachandran plot (%)		
Outliers	0.07	0.07

Allowed	7.55	9.70
Favored	92.39	90.23
Rama-Z (Ramachandran plot Z-score, RMSD)		
whole (N = 1484)	-1.53 (0.22)	-1.61 (0.22)
helix (N = 52)	-1.67 (0.67)	-1.45 (0.70)
sheet (N = 434)	-0.53 (0.25)	-0.59 (0.26)
loop (N = 998)	-1.25 (0.20)	-1.31 (0.20)
Rotamer outliers (%)	4.36	5.69
Cβ outliers (%)	0.00	0.00
Model vs. Data		
Cross Correlation (mask)	0.76	0.75
Cross Correlation (box)	0.84	0.86
Cross Correlation (peaks)	0.70	0.70
Cross Correlation (volume)	0.76	0.75
Mean CC for ligands	0.59	0.66

Table 7. Cryo-EM data collection, refinement and validation statistics.

6 Main figures

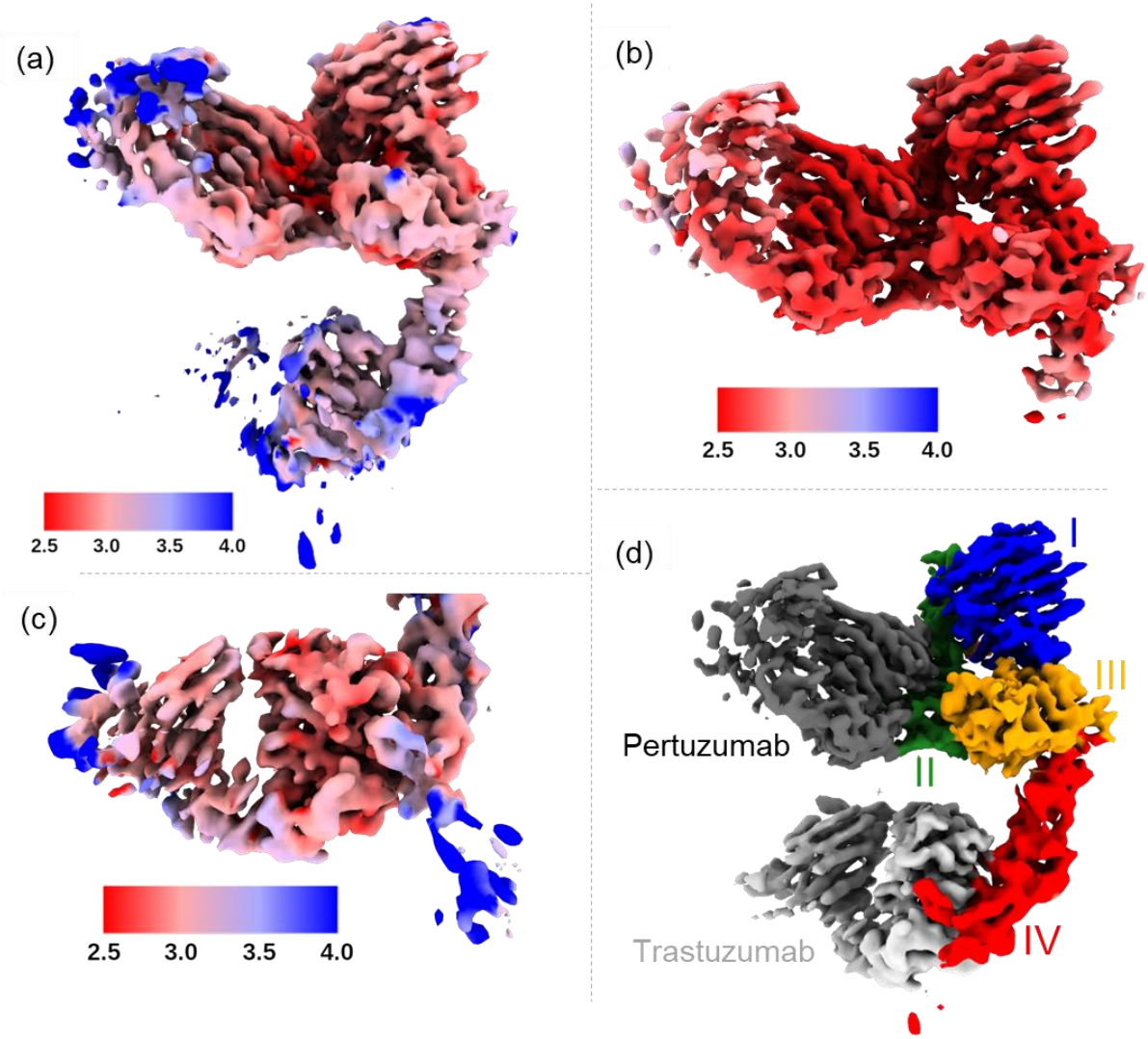

Figure 1: Baseline protocol vs focused and composite maps for the HTP complex. *Panel **(a)** shows the global map obtained from classic homogeneous refinement (baseline protocol). **(b)** and **(c)** maps are those obtained from focused refinements of the pertuzumab **(b)** and trastuzumab **(c)** regions. **(d)**, composite map combining the high resolution of the two local refinement maps (b,c) in one unique map. **(a)**, **(b)**, **(c)** are colored according to local resolution. **(d)** sHER2 is colored by domains (blue: I; green: II; yellow: III; red: IV), the pertuzumab Fab is colored in dark grey and the trastuzumab Fab in light grey.*

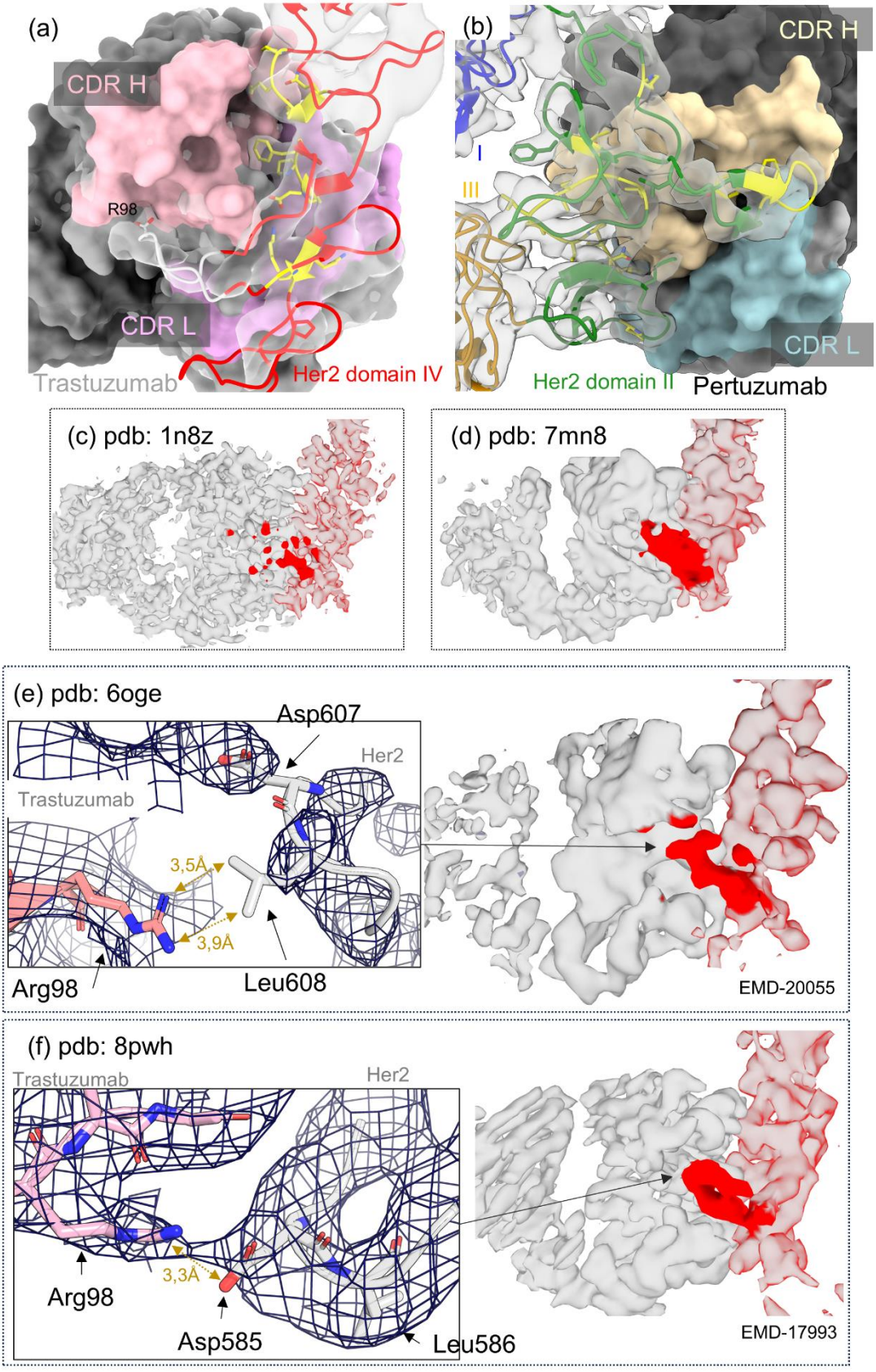

Figure 2: Pertuzumab and trastuzumab interfaces and overview of previously published maps. Panel **a** shows the i*nterface between HER2 and trastuzumab. Fab is shown as surface in grey (heavy chain) and light grey (light chain) with CDR's in pink (CDR H1-3) and purple (CDR L1-3). Experimental cryo-EM map of sHER2 is shown in*

transparent white. The four loops of the HER2 epitopes are in yellow for the three (557-561, 570-573, and 602-603) previously established (Cho *et al.*, 2003) *and in white for the fourth (581-593, this work). In red is the sHER2 domain IV.* ***b*** *shows the pertuzumab region. Fab is shown as surface in black (heavy chain) and light black (light chain) with CDR's in pale gold (CDR H1-3) and pale blue (CDR L1-3). Experimental cryo-EM map is shown in transparent white. sHER2 chain is colored by domains (blue for domain I, orange for domain II, and green for domain III).* ***c*** *is the x-ray map of 1n8z* [26]*,* ***d*** *the cryo-EM map of 7mn8 (HER2-HER3-NRG1β-trastuzumab complex)* [22]*,* ***e*** *the cryo-EM map of 6oge* [26]*, and* ***f*** *the focused cryo-EM map of Figure 1c (this work). The loop 581-590 that we propose to be considered as part of the trastuzumab epitope is shown in red in all maps, while sHER2 is in light red and Trastuzumab is colorless. Panels* ***e*** *and* ***f also*** *show the atomic reconstruction of the loop for each corresponding model. Maps are shown as mesh with contour level set to 6 at 4Å distance for 6oge and a contour of 11 and 3Å distance for 8pwh.*

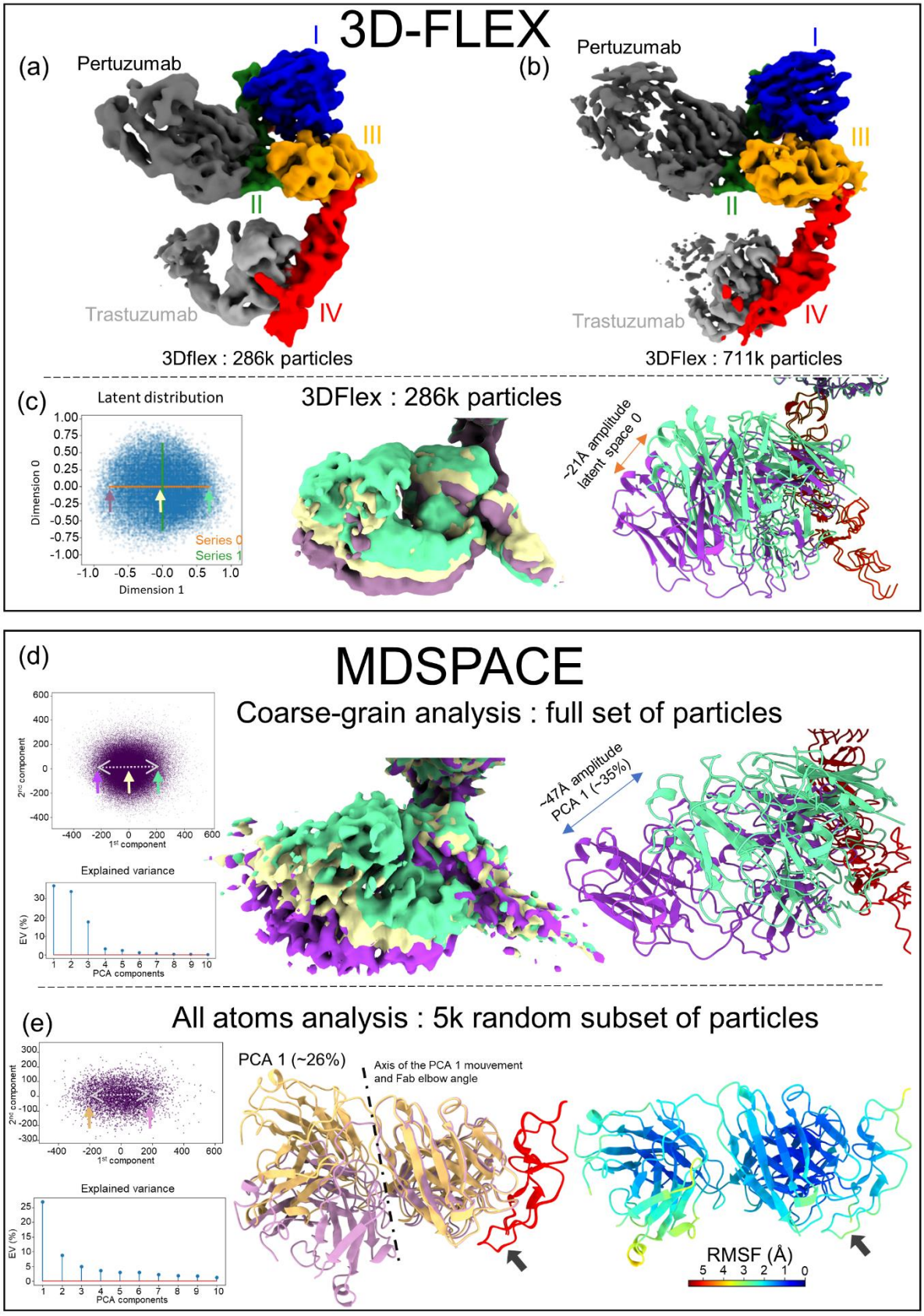

Figure 3: Continuous conformational variability analysis. (a) shows the 3D flex map obtained with the 286k subset of particles after RSPFilter screening, and **(b)** shows the 3DFlex map obtained using the full dataset of

particles. Both are colored by domain (I=Blue, II=Green, III=Orange, IV= Red). **(c)** shows the 286k subset 3Dflex conformational landscape visualization (left, orange line) resulting in an amplitude of motion of 21Å in the trastuzumab region. Note the loop density staying visible and moving collectively with the trastuzumab. **(d), (e) MDSPACE analysis**. **(d)**, analysis of the major motions using the full set of particles and a coarse-grained (Cα) HTP model. Left, principal component analysis: Bottom, variance explained by each principal component. Top, two-dimensional plot of the first two principal components. Right, 3D reconstructions and coarse-grained models: The fitted models and their corresponding maps for the first principal component extreme values after alignment to the pertuzumab region are shown, as well as one intermediate map (pale gold). Note that a large amplitude of motion of 47Å for trastuzumab+HER2 IV is found. **(e)**, local motion of the trastuzumab region, analyzed with a subset of 5000 particles and all-atom simulations with subsequent superposition on trastuzumab. Left, principal component analysis: Bottom, variance explained by each principal component. Top, two-dimensional plot of the first two principal components. Middle, two models showing the two extremes for the first principal component (26%) after alignment to the domain IV of sHER2. It shows the main motion is between the constant and variable parts of trastuzumab in accordance with the characteristic elbow angle of the fab. Right panel shows one of the models, in the same orientation as in the middle panel and colored by the root mean square fluctuation among the 5000 structures. The 581-590 loop is shown with a black arrow in the middle and right panels.

7 Supplementary figures

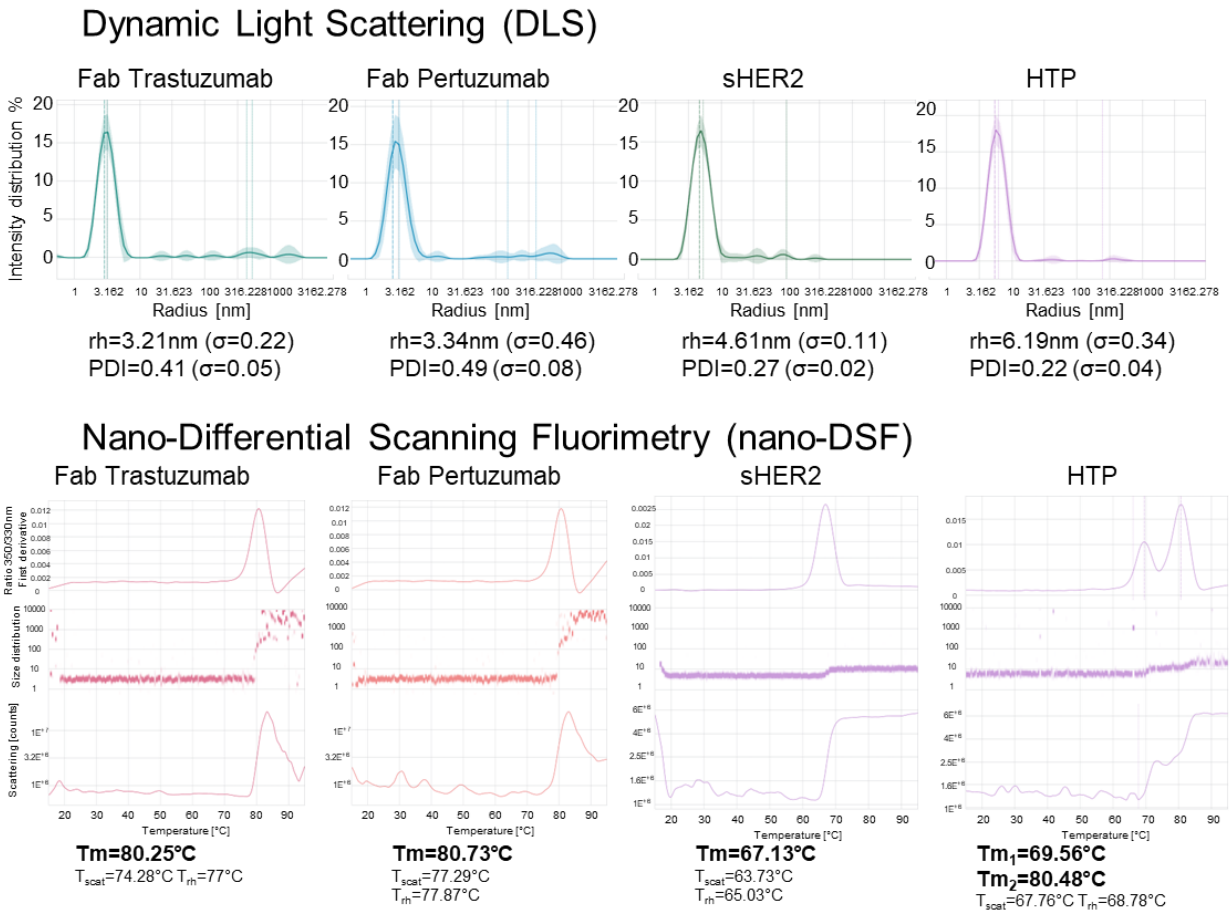

Supplementary figure 1. Biophysical sample characterization. *DLS, nano-DSF, SEC-SLS and Mass-photometry measurements. DLS and Nano-DSF show typical results for each Fabs, sHER2 and the HTP complex. The SEC-SLS panel shows the result of the SLS using HTP.*

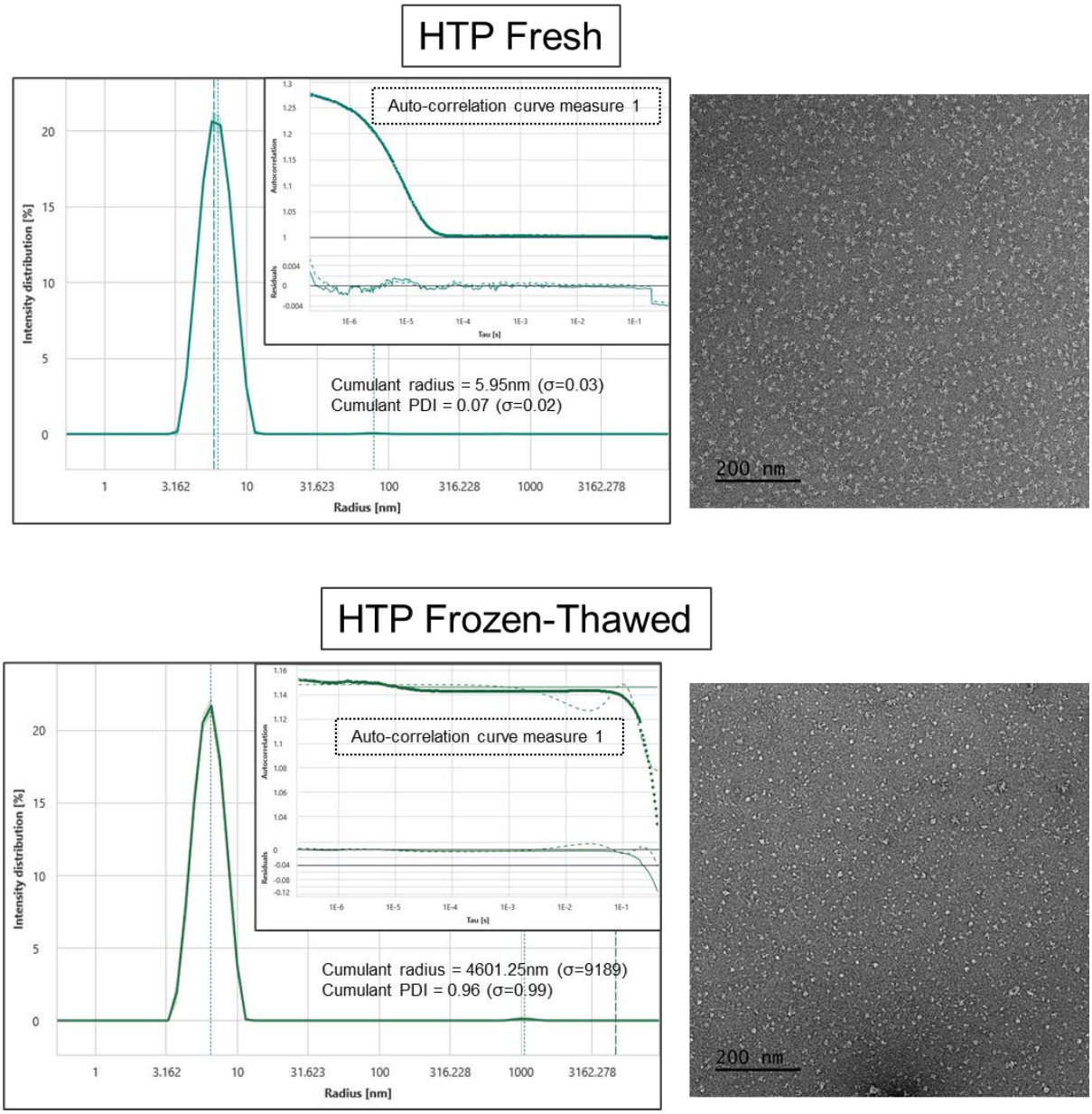

Supplementary figure 2. *Sample DLS measurement (nanotemper panta) and negative staining comparison of the same sample before and after flash-frozen/thawed cycle.*

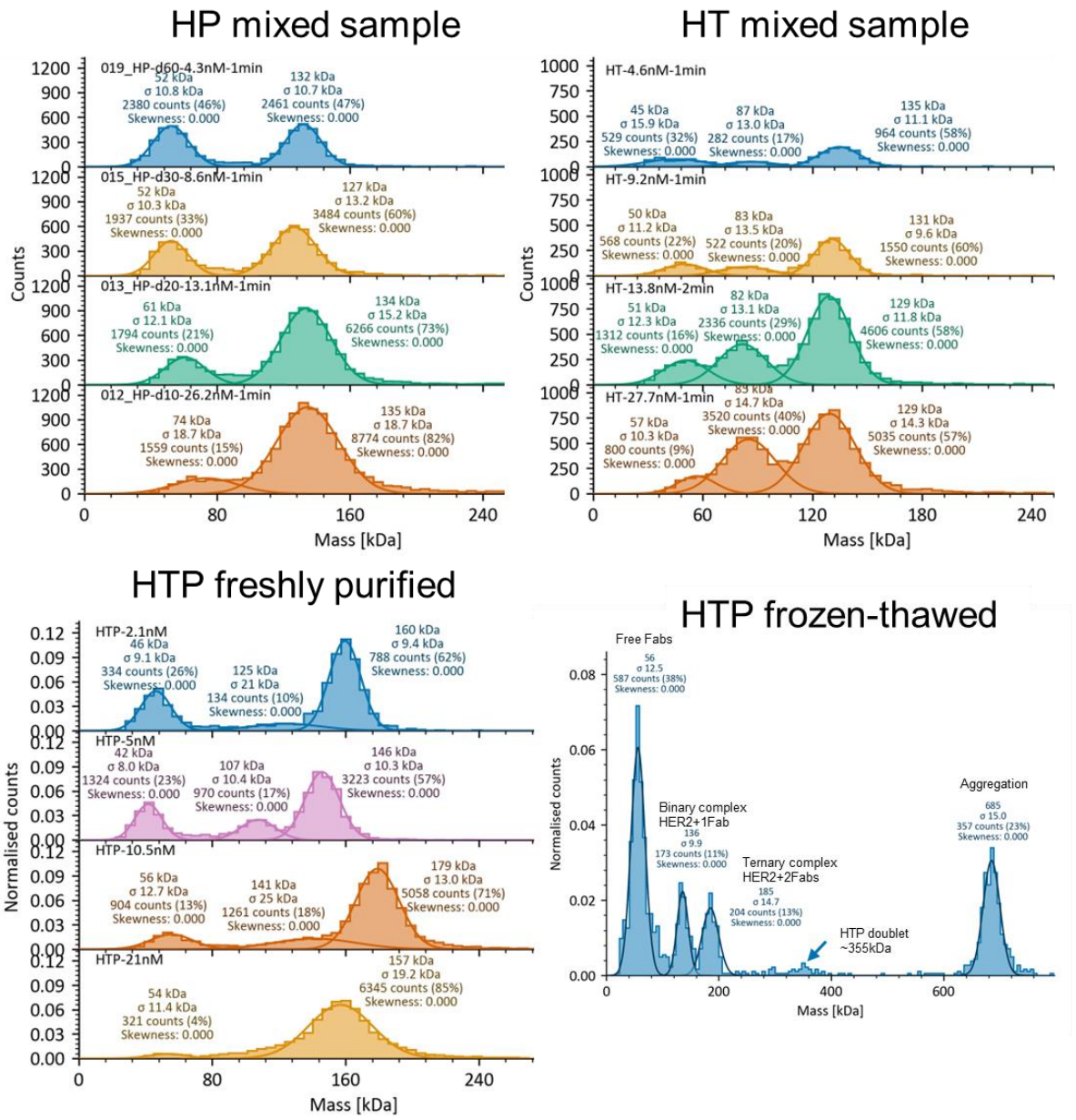

Supplementary figure 3. *Summary of mass photometry experiments. HP = HER2-pertuzumab Fab, HT= HER2-trastuzumab Fab. The two series of measurements HT and HP (top) were performed by mixing the two partners before starting the experiment. The HTP freshly purified measurements (bottom left) were done with a sample purified on the same day. The bottom right measurement was performed on an old frozen-thawed sample.*

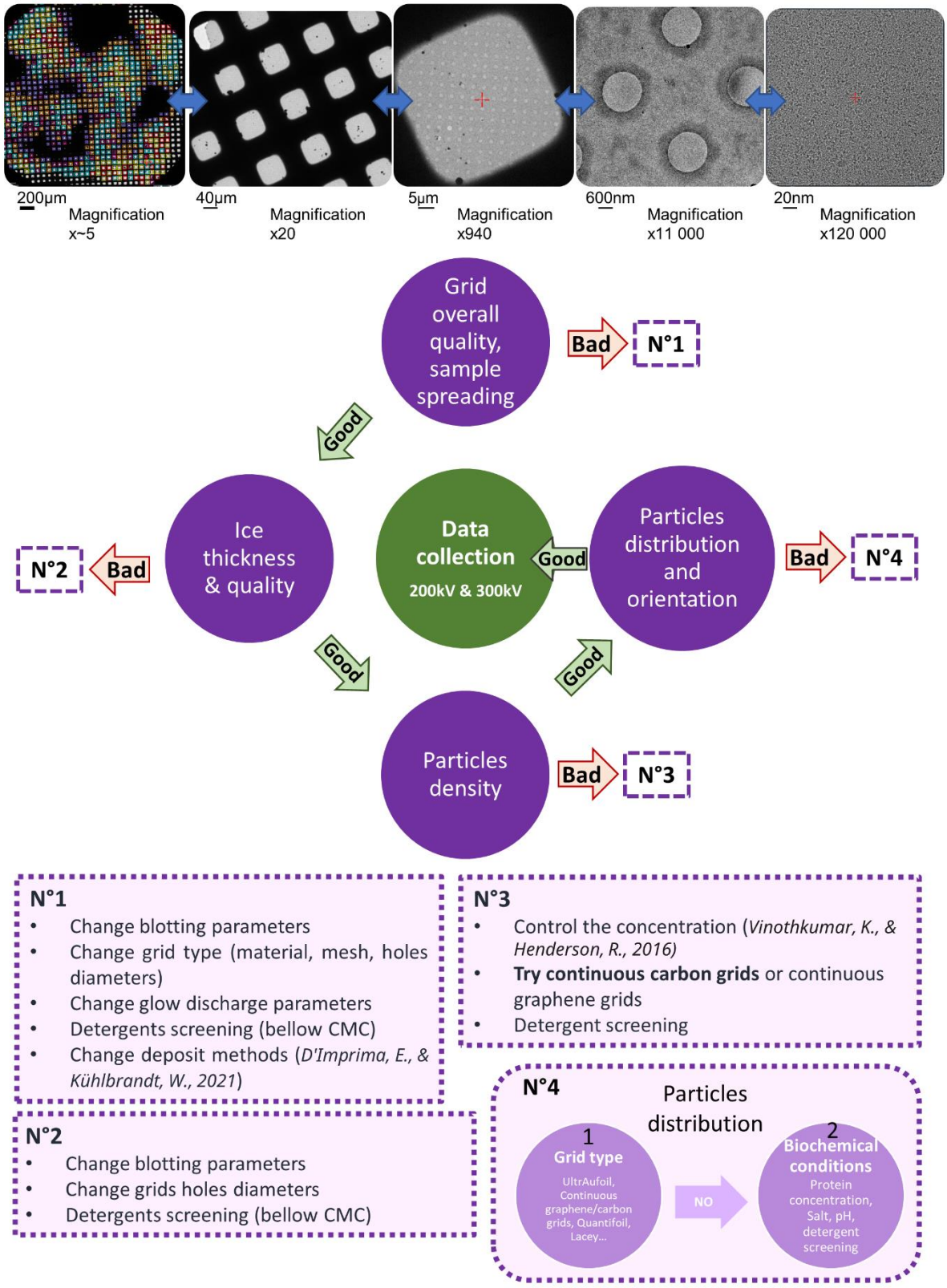

Supplementary figure 4. *Synthetic pipeline for grids screening and decision tree for troubleshooting.*

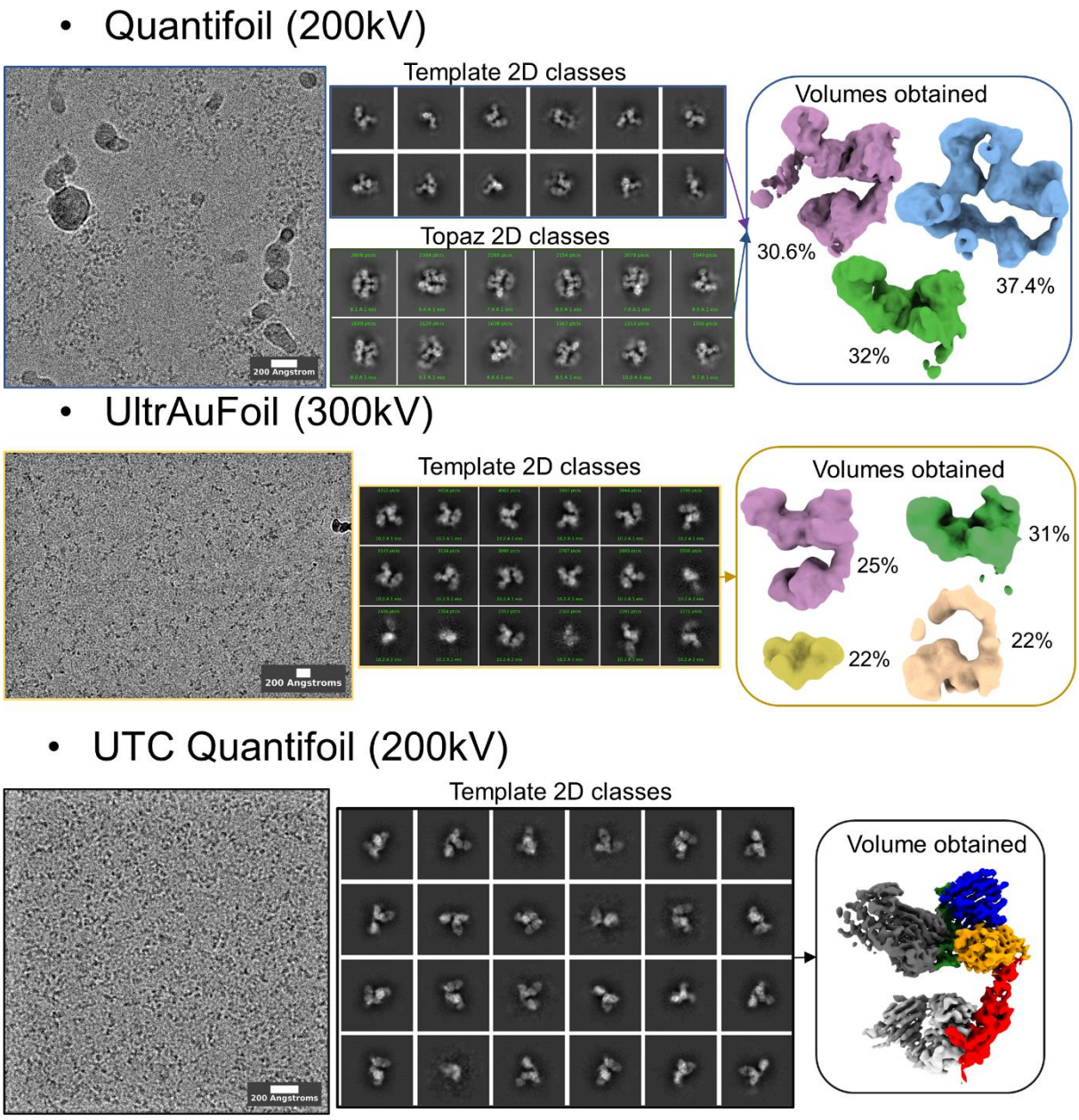

Supplementary figure 5. *To the left is shown a typical micrograph aspect, in the middle some representative 2D classes and to the right the volumes obtained according to the grids used. Upper volumes were obtained when using QF 1.2/1.3µm grids. The violet is the classic HTP trimer. However, it is worth noting that 3D classification (without alignment) with particles of this class reveal a strong heterogeneity (not shown). The doublet is in blue and the partial complex (likely pertuzumab/sHER2) is in green. Middle panel correspond to data obtained when using UF 0.6/1µm, two volumes can be identified with good confidence as the HTP in violet and the partial complex in green. Two others are more difficult to assign but could arise from strongly deteriorated particles such as Fab and trastuzumab/sHER2 or other. Lower panels correspond to data obtained when using UTC quantifoil 1.2/1.3µm. Sample appear highly homogeneous, and a high-resolution map could be obtained without any trace of dissociated complex.*

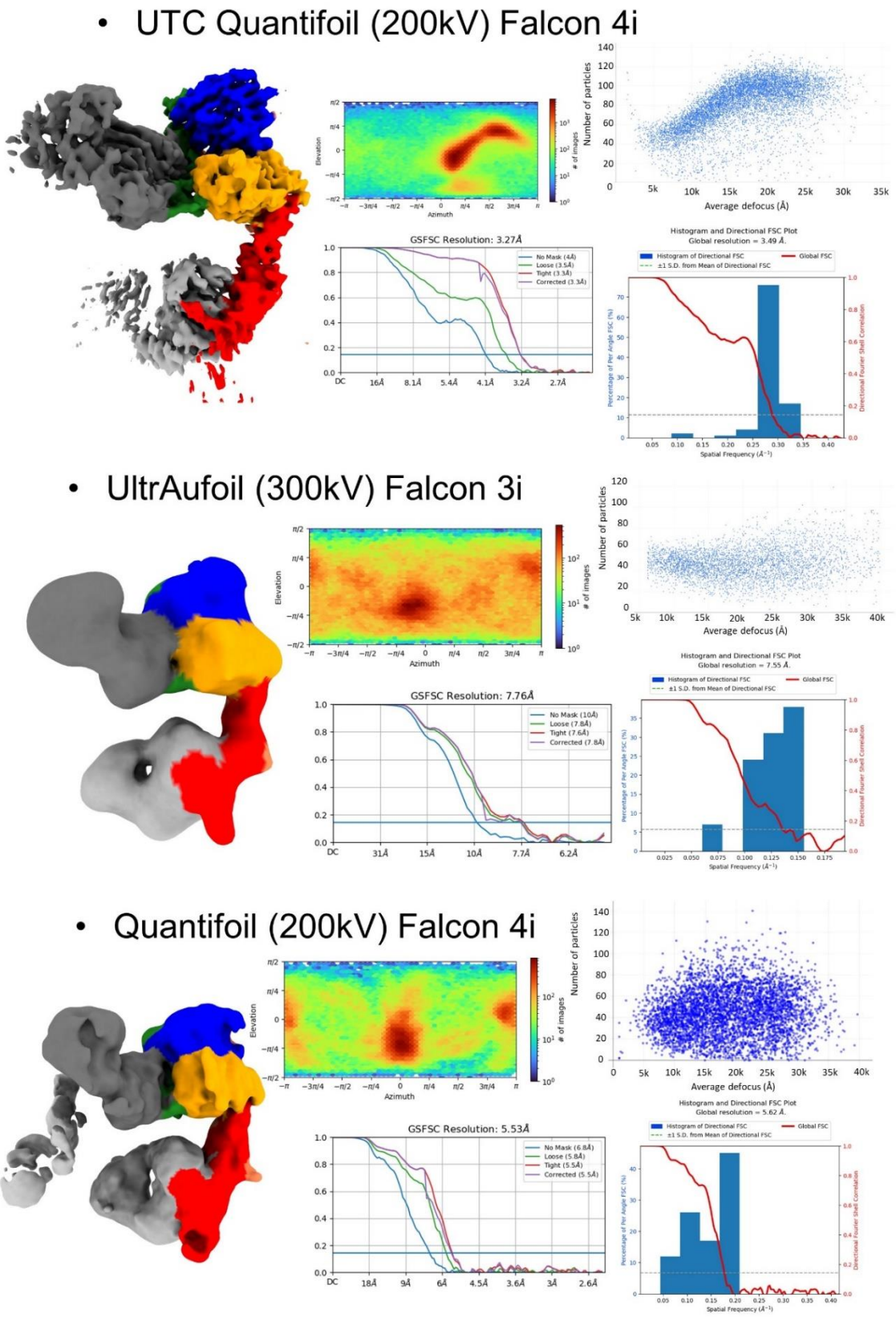

Supplementary figure 6. *Summary of the three reconstructions showing the HTP complex described in this paper. For each grid the HTP map is shown with sHER2 colored by domain and Fab in grey. Orientation distribution and FSC curve are given in the center. To the right the distribution of average defoci of particles contributing to the reconstruction of the volume and the 3D-FSC analysis as output by cryoSPARC.*

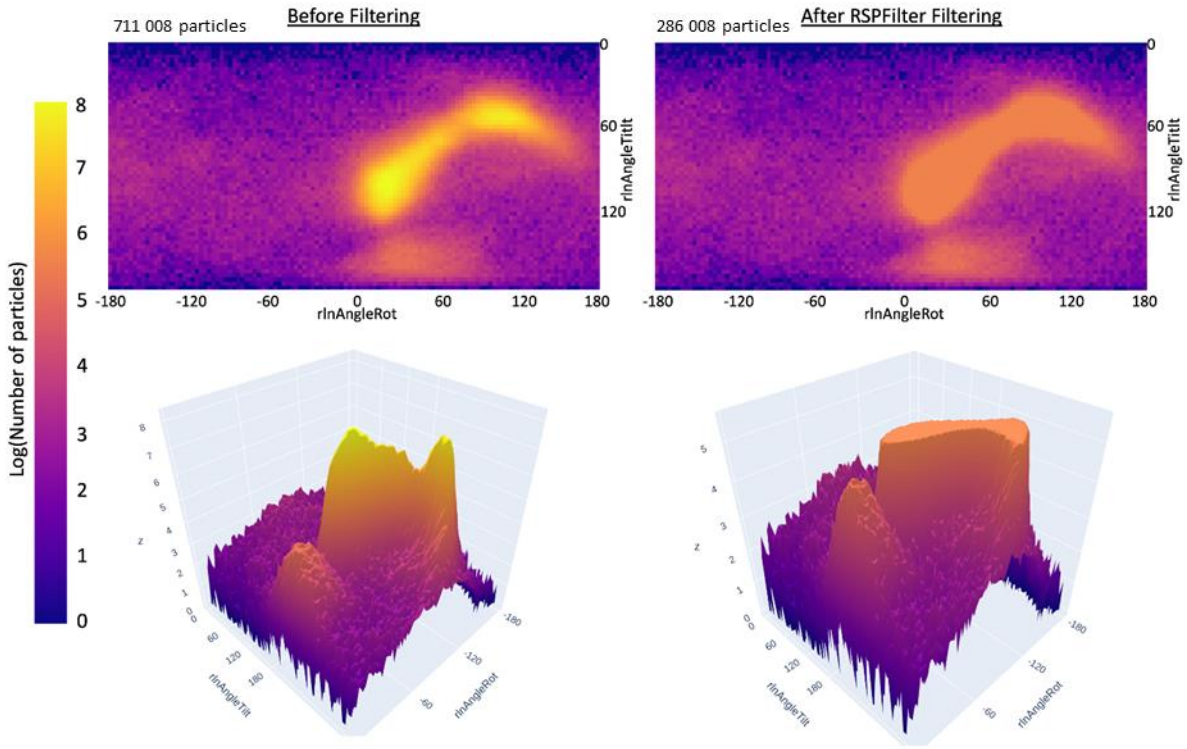

Supplementary figure 7. Particle angular distribution from the global refinement before and after RSPFilter filtering*. Left is the angular distribution 2D plot of the dataset before RSPFilter clean-up and right is after clean-up. Lower panels show the same plots visualized in 3D. The logarithmic scale color is the same for all plots (2D and 3D). Only the particles from the more represented views are removed without impacting the rare views of the object.*

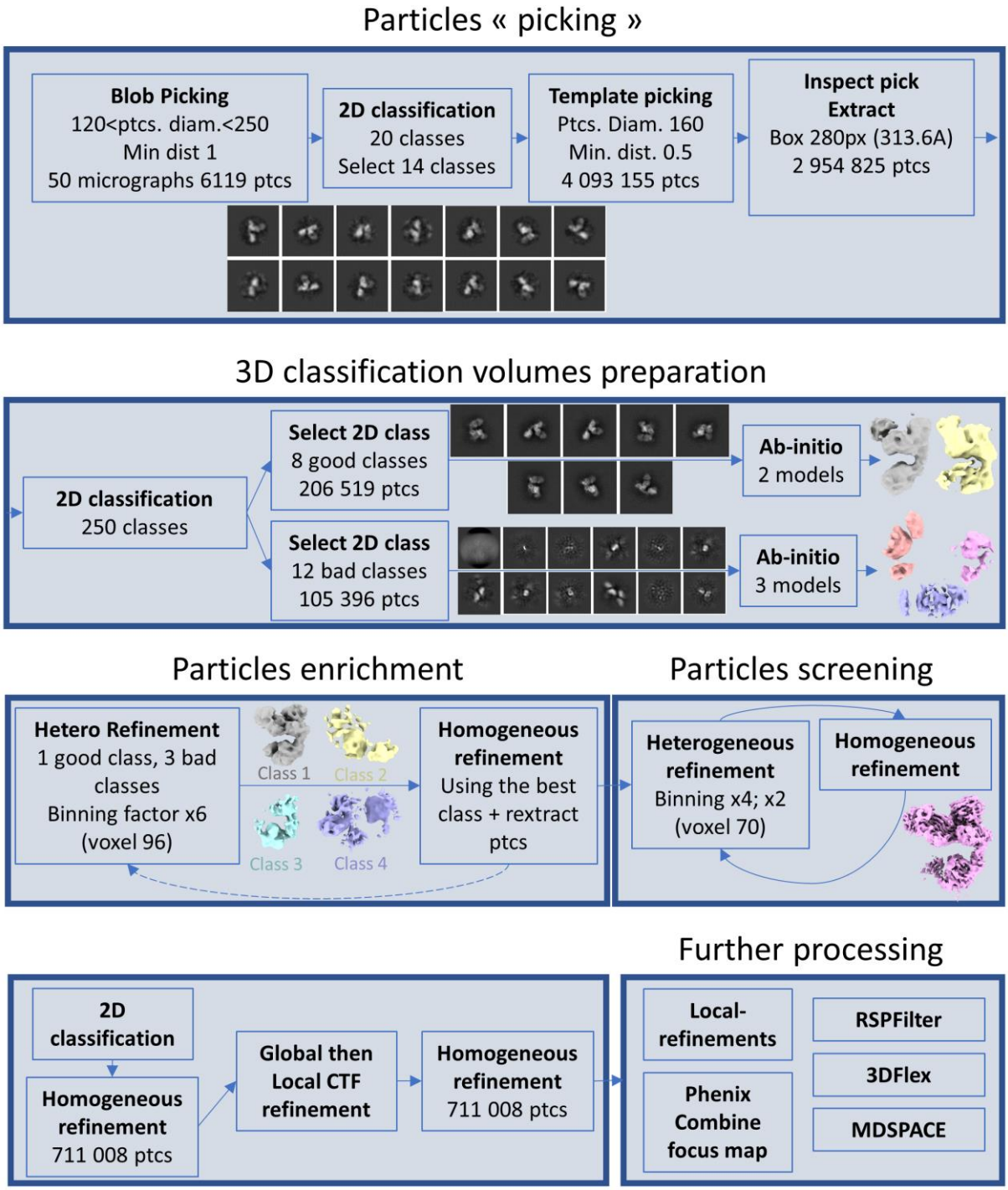

Supplementary figure 8. *Overview of the data processing strategy used for the UTC-Quantifoil grid.*

8 References

[1] M.A. Olayioye, R.M. Neve, H.A. Lane, N.E. Hynes, The ErbB signaling network: receptor heterodimerization in development and cancer, Embo J. 19 (2000) 3159–3167. https://doi.org/10.1093/emboj/19.13.3159.

[2] D.B. Peckys, U. Korf, N. de Jonge, Local variations of HER2 dimerization in breast cancer cells discovered by correlative fluorescence and liquid electron microscopy, Sci Adv. 1 (2015) e1500165. https://doi.org/10.1126/sciadv.1500165.

[3] R. Ghosh, A. Narasanna, S.E. Wang, S. Liu, A. Chakrabarty, J.M. Balko, A.M. González-Angulo, G.B. Mills, E. Penuel, J. Winslow, J. Sperinde, R. Dua, S. Pidaparthi, A. Mukherjee, K. Leitzel, W.J. Kostler, A. Lipton, M. Bates, C.L. Arteaga, Trastuzumab Has Preferential Activity against Breast Cancers Driven by HER2 Homodimers, Cancer Res. 71 (2011) 1871–1882. https://doi.org/10.1158/0008-5472.can-10-1872.

[4] D. Karunagaran, E. Tzahar, R.R. Beerli, X. Chen, D. Graus-Porta, B.J. Ratzkin, R. Seger, N.E. Hynes, Y. Yarden, ErbB-2 is a common auxiliary subunit of NDF and EGF receptors: implications for breast cancer., Embo J. 15 (1996) 254–64.

[5] D. Graus-Porta, R.R. Beerli, J.M. Daly, N.E. Hynes, ErbB-2, the preferred heterodimerization partner of all ErbB receptors, is a mediator of lateral signaling, Embo J. 16 (1997) 1647–1655. https://doi.org/10.1093/emboj/16.7.1647.

[6] FDA, Herceptin (trastuzumab) FDA Approval History - Drugs.com, (1998). https://www.drugs.com/history/herceptin.html (accessed May 30, 2023).

[7] E.M.A. EMA, Herceptin | European Medicines Agency, (2000). https://www.ema.europa.eu/en/medicines/human/EPAR/herceptin (accessed April 25, 2023).

[8] T. Ben-Kasus, B. Schechter, S. Lavi, Y. Yarden, M. Sela, Persistent elimination of ErbB-2/HER2-overexpressing tumors using combinations of monoclonal antibodies: Relevance of receptor endocytosis, Proc. Natl. Acad. Sci. 106 (2009) 3294–3299. https://doi.org/10.1073/pnas.0812059106.

[9] M.A. Molina, J. Codony-Servat, J. Albanell, F. Rojo, J. Arribas, J. Baselga, Trastuzumab (herceptin), a humanized anti-Her2 receptor monoclonal antibody, inhibits basal and activated Her2 ectodomain cleavage in breast cancer cells., Cancer Res. 61 (2001) 4744–9.

[10] P.R. Pohlmann, I.A. Mayer, R. Mernaugh, Resistance to Trastuzumab in Breast Cancer, Clin Cancer Res. 15 (2009) 7479–7491. https://doi.org/10.1158/1078-0432.ccr-09-0636.

[11] F. and D.A. FDA, Perjeta: Uses, Dosage, Side Effects & Warnings - Drugs.com, (2012). https://www.drugs.com/perjeta.html (accessed May 30, 2023).

[12] E.M.A. EMA, Perjeta | European Medicines Agency, (2013). https://www.ema.europa.eu/en/medicines/human/EPAR/perjeta (accessed May 30, 2023).

[13] B. Nami, H. Maadi, Z. Wang, Mechanisms Underlying the Action and Synergism of Trastuzumab and Pertuzumab in Targeting HER2-Positive Breast Cancer, Cancers. 10 (2018) 342. https://doi.org/10.3390/cancers10100342.

[14] R. Nahta, M.-C. Hung, F.J. Esteva, The HER-2-Targeting Antibodies Trastuzumab and Pertuzumab Synergistically Inhibit the Survival of Breast Cancer Cells, Cancer Res. 64 (2004) 2343–2346. https://doi.org/10.1158/0008-5472.can-03-3856.

[15] S. Richard, F. Selle, J.-P. Lotz, A. Khalil, J. Gligorov, D.G. Soares, Pertuzumab and trastuzumab: the rationale way to synergy, An. Da Acad. Bras. Ciências. 88 (2016) 565–577. https://doi.org/10.1590/0001-3765201620150178.

[16] W. Scheuer, T. Friess, H. Burtscher, B. Bossenmaier, J. Endl, M. Hasmann, Strongly Enhanced Antitumor Activity of Trastuzumab and Pertuzumab Combination Treatment on HER2-Positive Human Xenograft Tumor Models, Cancer Res. 69 (2009) 9330–9336. https://doi.org/10.1158/0008-5472.can-08-4597.

[17] G.M. Blumenthal, N.S. Scher, P. Cortazar, S. Chattopadhyay, S. Tang, P. Song, Q. Liu, K. Ringgold, A.M. Pilaro, A. Tilley, K.E. King, L. Graham, B.L. Rellahan, W.C. Weinberg, B. Chi, C. Thomas, P. Hughes, A. Ibrahim, R. Justice, R. Pazdur, First FDA Approval of Dual Anti-HER2 Regimen: Pertuzumab in Combination with Trastuzumab and Docetaxel for HER2-Positive Metastatic Breast Cancer, Clin Cancer Res. 19 (2013) 4911–4916. https://doi.org/10.1158/1078-0432.ccr-13-1212.

[18] L.J. Howie, N.S. Scher, L. Amiri-Kordestani, L. Zhang, B.L. King-Kallimanis, Y. Choudhry, J. Schroeder, K.B. Goldberg, P.G. Kluetz, A. Ibrahim, R. Sridhara, G.M. Blumenthal, R. Pazdur, J.A. Beaver, FDA Approval Summary: Pertuzumab for Adjuvant Treatment of HER2-Positive Early Breast Cancer, Clin Cancer Res. 25 (2019) 2949–2955. https://doi.org/10.1158/1078-0432.ccr-18-3003.

[19] X. Liu, Y. Fang, Y. Li, Y. Li, L. Qi, X. Wang, Pertuzumab combined with trastuzumab compared to trastuzumab in the treatment of HER2-positive breast cancer: A systematic review and meta-analysis of randomized controlled trials, Frontiers Oncol. 12 (2022) 894861. https://doi.org/10.3389/fonc.2022.894861.

[20] H.-S. Cho, K. Mason, K.X. Ramyar, A.M. Stanley, S.B. Gabelli, D.W. Denney, D.J. Leahy, Structure of the extracellular region of HER2 alone and in complex with the Herceptin Fab, Nature. 421 (2003) 756–760. https://doi.org/10.1038/nature01392.

[21] M.C. Franklin, K.D. Carey, F.F. Vajdos, D.J. Leahy, A.M. de Vos, M.X. Sliwkowski, Insights into ErbB signaling from the structure of the ErbB2-pertuzumab complex, Cancer Cell. 5 (2004) 317–328. https://doi.org/10.1016/s1535-6108(04)00083-2.

[22] D. Diwanji, R. Trenker, T.M. Thaker, F. Wang, D.A. Agard, K.A. Verba, N. Jura, Structures of the HER2–HER3–NRG1β complex reveal a dynamic dimer interface, Nature. 600 (2021) 339–343. https://doi.org/10.1038/s41586-021-04084-z.

[23] X. Bai, P. Sun, X. Wang, C. Long, S. Liao, S. Dang, S. Zhuang, Y. Du, X. Zhang, N. Li, K. He, Z. Zhang, Structure and dynamics of the EGFR/HER2 heterodimer, Cell Discov. 9 (2023) 18. https://doi.org/10.1038/s41421-023-00523-5.

[24] R. Vuillemot, A. Mirzaei, M. Harastani, I. Hamitouche, L. Fréchin, B.P. Klaholz, O. Miyashita, F. Tama, I. Rouiller, S. Jonic, MDSPACE: Extracting continuous conformational landscapes from cryo-EM single particle datasets using 3D-to-2D flexible fitting based on Molecular Dynamics simulation, J Mol Biol. (2023) 167951. https://doi.org/10.1016/j.jmb.2023.167951.

[25] A. Punjani, D.J. Fleet, 3D Flexible Refinement: Structure and Motion of Flexible Proteins from Cryo-EM, Biorxiv. (2021) 2021.04.22.440893. https://doi.org/10.1101/2021.04.22.440893.

[26] Y. Hao, X. Yu, Y. Bai, H.J. McBride, X. Huang, Cryo-EM Structure of HER2-trastuzumab-pertuzumab complex, Plos One. 14 (2019) e0216095. https://doi.org/10.1371/journal.pone.0216095.

[27] L.A. Passmore, C.J. Russo, Chapter Three Specimen Preparation for High-Resolution Cryo-EM, Methods Enzymol. 579 (2016) 51–86. https://doi.org/10.1016/bs.mie.2016.04.011.

[28] G. Weissenberger, R.J.M. Henderikx, P.J. Peters, Understanding the invisible hands of sample preparation for cryo-EM, Nat Methods. 18 (2021) 463–471. https://doi.org/10.1038/s41592-021-01130-6.

[29] H.G. Brown, E. Hanssen, MeasureIce: accessible on-the-fly measurement of ice thickness in cryo-electron microscopy, Commun Biology. 5 (2022) 817. https://doi.org/10.1038/s42003-022-03698-x.

[30] K.R. Vinothkumar, R. Henderson, Single particle electron cryomicroscopy: trends, issues and future perspective, Q Rev Biophys. 49 (2016) e13. https://doi.org/10.1017/s0033583516000068.

[31] W.J. Rice, A. Cheng, A.J. Noble, E.T. Eng, L.Y. Kim, B. Carragher, C.S. Potter, Routine determination of ice thickness for cryo-EM grids, J Struct Biol. 204 (2018) 38–44. https://doi.org/10.1016/j.jsb.2018.06.007.

[32] J. Chen, A.J. Noble, J.Y. Kang, S.A. Darst, Eliminating effects of particle adsorption to the air/water interface in single-particle cryo-electron microscopy: Bacterial RNA polymerase and CHAPSO, J. Struct. Biol.: X. 1 (2019) 100005. https://doi.org/10.1016/j.yjsbx.2019.100005.

[33] D. Kampjut, J. Steiner, L.A. Sazanov, Cryo-EM grid optimization for membrane proteins, Iscience. 24 (2021) 102139. https://doi.org/10.1016/j.isci.2021.102139.

[34] R.M. Glaeser, Proteins, interfaces, and cryo-EM grids, Curr. Opin. Colloid Interface Sci. 34 (2018) 1–8. https://doi.org/10.1016/j.cocis.2017.12.009.

[35] N. Berrow, A. de Marco, M. Lebendiker, M. Garcia-Alai, S.H. Knauer, B. Lopez-Mendez, A. Matagne, A. Parret, K. Remans, S. Uebel, B. Raynal, Quality control of purified proteins to improve data quality and reproducibility: results from a large-scale survey, Eur Biophys J. 50 (2021) 453–460. https://doi.org/10.1007/s00249-021-01528-2.

[36] B. Raynal, S. Brûlé, S. Uebel, S.H. Knauer, Protein-Ligand Interactions, Methods and Applications, Methods Mol Biology. 2263 (2021) 3–46. https://doi.org/10.1007/978-1-0716-1197-5_1.

[37] A. Sonn-Segev, K. Belacic, T. Bodrug, G. Young, R.T. VanderLinden, B.A. Schulman, J. Schimpf, T. Friedrich, P.V. Dip, T.U. Schwartz, B. Bauer, J.-M. Peters, W.B. Struwe, J.L.P. Benesch, N.G. Brown, D. Haselbach, P. Kukura, Quantifying the heterogeneity of macromolecular machines by mass photometry, Nat Commun. 11 (2020) 1772. https://doi.org/10.1038/s41467-020-15642-w.

[38] W. Fu, Y. Wang, Y. Zhang, L. Xiong, H. Takeda, L. Ding, Q. Xu, L. He, W. Tan, A.N. Bethune, L. Zhou, Insights into HER2 signaling from step-by-step optimization of anti-HER2 antibodies, Mabs. 6 (2014) 978–990. https://doi.org/10.4161/mabs.28786.

[39] W.-L. Ling, W.-H. Lua, J.-J. Poh, J.Y. Yeo, D.P. Lane, S.K.-E. Gan, Effect of VH–VL Families in Pertuzumab and Trastuzumab Recombinant Production, Her2 and FcγIIA Binding, Front Immunol. 9 (2018) 469. https://doi.org/10.3389/fimmu.2018.00469.

[40] A. Punjani, J.L. Rubinstein, D.J. Fleet, M.A. Brubaker, cryoSPARC: algorithms for rapid unsupervised cryo-EM structure determination, Nat Methods. 14 (2017) 290–296. https://doi.org/10.1038/nmeth.4169.

[41] T.P.J. Garrett, N.M. McKern, M. Lou, T.C. Elleman, T.E. Adams, G.O. Lovrecz, H.-J. Zhu, F. Walker, M.J. Frenkel, P.A. Hoyne, R.N. Jorissen, E.C. Nice, A.W. Burgess, C.W. Ward, Crystal Structure of a Truncated Epidermal Growth Factor Receptor Extracellular Domain Bound to Transforming Growth Factor α, Cell. 110 (2002) 763–773. https://doi.org/10.1016/s0092-8674(02)00940-6.

[42] Z.-H. Wang, Z.-Q. Zheng, S.C. Jia, S.-N. Liu, X.-F. Xiao, G.-Y. Chen, W.-Q. Liang, X.-F. Lu, Trastuzumab resistance in HER2-positive breast cancer: Mechanisms, emerging biomarkers and targeting agents, Front Oncol 12 (2022) 1006429. https://doi.org/10.3389/fonc.2022.1006429.

[43] L. Castagnoli, M. Ladomery, E. Tagliabue, S.M. Pupa, The d16HER2 Splice Variant: A Friend or Foe of HER2-Positive Cancers?, Cancers (Basel) 11 (2019) 902. https://doi.org/10.3390/cancers11070902.

[44] F. Soltermann, E.D.B. Foley, V. Pagnoni, M. Galpin, J.L.P. Benesch, P. Kukura, W.B. Struwe, Quantifying Protein–Protein Interactions by Molecular Counting with Mass Photometry, Angew. Chem. Int. Ed. 59 (2020) 10774–10779. https://doi.org/10.1002/anie.202001578.

[45] P. Virtanen, R. Gommers, T.E. Oliphant, M. Haberland, T. Reddy, D. Cournapeau, E. Burovski, P. Peterson, W. Weckesser, J. Bright, S.J. van der Walt, M. Brett, J. Wilson, K.J. Millman, N. Mayorov, A.R.J. Nelson, E. Jones, R. Kern, E. Larson, C.J. Carey, İ. Polat, Y. Feng, E.W. Moore, J. VanderPlas, D. Laxalde, J. Perktold, R. Cimrman, I. Henriksen, E.A. Quintero, C.R. Harris, A.M. Archibald, A.H. Ribeiro, F. Pedregosa, P. van Mulbregt, S. 1 0 Contributors, A. Vijaykumar, A.P. Bardelli, A. Rothberg, A. Hilboll, A. Kloeckner, A. Scopatz, A. Lee, A. Rokem, C.N. Woods, C. Fulton, C. Masson, C. Häggström, C. Fitzgerald, D.A. Nicholson, D.R. Hagen, D.V. Pasechnik, E. Olivetti, E. Martin, E. Wieser, F. Silva, F. Lenders, F. Wilhelm, G. Young, G.A. Price, G.-L. Ingold, G.E. Allen, G.R. Lee, H. Audren, I. Probst, J.P. Dietrich, J. Silterra, J.T. Webber, J. Slavič, J. Nothman, J. Buchner, J. Kulick, J.L. Schönberger, J.V. de M. Cardoso, J. Reimer, J. Harrington, J.L.C. Rodríguez, J. Nunez-Iglesias, J. Kuczynski, K. Tritz, M. Thoma, M. Newville, M. Kümmerer, M. Bolingbroke, M. Tartre, M. Pak, N.J. Smith, N. Nowaczyk, N. Shebanov, O. Pavlyk, P.A. Brodtkorb, P. Lee, R.T. McGibbon, R. Feldbauer, S. Lewis, S. Tygier, S. Sievert, S. Vigna, S. Peterson, S. More, T. Pudlik, T. Oshima, T.J. Pingel, T.P. Robitaille, T. Spura, T.R. Jones, T. Cera, T. Leslie, T. Zito, T. Krauss, U. Upadhyay, Y.O. Halchenko, Y. Vázquez-Baeza, SciPy 1.0: fundamental algorithms for scientific computing in Python, Nat Methods. 17 (2020) 261–272. https://doi.org/10.1038/s41592-019-0686-2.

[46] Plotly, Collaborative data science, 2015. https://plot.ly.

[47] T. Tubiana, RSPFilter, Zenodo. (2022). https://doi.org/10.5281/zenodo.7413914.

[48] D. Asarnow, E. Palovcak, & Y. Cheng, UCSF pyem, Zenodo. (2019). https://doi.org/10.5281/zenodo.3576630.

[49] C. Kobayashi, J. Jung, Y. Matsunaga, T. Mori, T. Ando, K. Tamura, M. Kamiya, Y. Sugita, GENESIS 1.1: A hybrid-parallel molecular dynamics simulator with enhanced sampling algorithms on multiple computational platforms, J. Comput. Chem. 38 (2017) 2193–2206. https://doi.org/10.1002/jcc.24874.

[50] R. Vuillemot, O. Miyashita, F. Tama, I. Rouiller, S. Jonic, NMMD: Efficient Cryo-EM Flexible Fitting Based on Simultaneous Normal Mode and Molecular Dynamics atomic displacements, J Mol Biol. 434 (2022) 167483. https://doi.org/10.1016/j.jmb.2022.167483.

[51] J.M. de la Rosa-Trevín, A. Quintana, L. del Cano, A. Zaldívar, I. Foche, J. Gutiérrez, J. Gómez-Blanco, J. Burguet-Castell, J. Cuenca-Alba, V. Abrishami, J. Vargas, J. Otón, G. Sharov, J.L. Vilas, J. Navas, P. Conesa, M. Kazemi, R. Marabini, C.O.S. Sorzano, J.M. Carazo, Scipion: A software framework toward integration, reproducibility and validation in

3D electron microscopy, J Struct Biol. 195 (2016) 93–99. https://doi.org/10.1016/j.jsb.2016.04.010.

[52] M. Harastani, R. Vuillemot, I. Hamitouche, N.B. Moghadam, S. Jonic, ContinuousFlex: Software package for analyzing continuous conformational variability of macromolecules in cryo electron microscopy and tomography data, J Struct Biol. 214 (2022) 107906. https://doi.org/10.1016/j.jsb.2022.107906.

[53] T. Bepler, A. Morin, M. Rapp, J. Brasch, L. Shapiro, A.J. Noble, B. Berger, Positive-unlabeled convolutional neural networks for particle picking in cryo-electron micrographs, Nat Methods. 16 (2019) 1153–1160. https://doi.org/10.1038/s41592-019-0575-8.

[54] T.I. Croll, ISOLDE: a physically realistic environment for model building into low-resolution electron-density maps, Acta Crystallogr Sect D Struct Biology. 74 (2018) 519–530. https://doi.org/10.1107/s2059798318002425.

[55] E.F. Pettersen, T.D. Goddard, C.C. Huang, E.C. Meng, G.S. Couch, T.I. Croll, J.H. Morris, T.E. Ferrin, UCSF ChimeraX: Structure visualization for researchers, educators, and developers, Protein Sci. 30 (2021) 70–82. https://doi.org/10.1002/pro.3943.

[56] J. Bostrom, S.-F. Yu, D. Kan, B.A. Appleton, C.V. Lee, K. Billeci, W. Man, F. Peale, S. Ross, C. Wiesmann, G. Fuh, Variants of the Antibody Herceptin That Interact with HER2 and VEGF at the Antigen Binding Site, Science. 323 (2009) 1610–1614. https://doi.org/10.1126/science.1165480.